In situ measurement of atmospheric krypton and xenon on Mars with Mars Science Laboratory

Authors: P. G. Conrad[1], C. A. Malespin[1, 2], H. B. Franz[1, 3], R. O. Pepin[4], M. G. Trainer[1], S. P. Schwenzer[5], S. K. Atreya[6], C. Freissinet[1], J. H. Jones[7], H. Manning[8], T. Owen[9], A. A. Pavlov[1], R. C. Wiens[10], M. H. Wong[6] and P.R. Mahaffy[1]

Affiliations:

[1]Solar System Exploration Division, NASA Goddard Space Flight Center, Greenbelt, MD 20771, USA.

[2]Universities Space Research Association (USRA), Columbia, MD USA

[3]CRESST, UMBC, NASA GSFC, Greenbelt, MD 20771 USA

[4]University of Minnesota, Minneapolis, MN 55455, USA

[5]The Open University, Department for Environment, Earth and Ecosystems, Walton Hall, Milton Keynes MK6 3AQ, United Kingdom.

[6]Climate and Space Sciences and Engineering, University of Michigan, Ann Arbor, MI 48109-2143, USA.

[7]XI-3, ARES, NASA/JSC, Houston, TX 770 58 USA

[8]Concordia University, Moorhead, MN 56562 USA

[9]University of Hawaii, Honolulu, HI 96822 USA

[10]Los Alamos National Laboratory, Los Alamos NM 87545 USA

***Correspondence to:** Pamela.G.Conrad@nasa.gov

Abstract Mars Science Laboratory's Sample Analysis at Mars (SAM) investigation has measured all of the stable isotopes of the heavy noble gases krypton and xenon in the martian atmosphere, *in situ*, from the Curiosity Rover at Gale Crater, Mars. Previous knowledge of martian atmospheric krypton and xenon isotope ratios has been based upon a combination of the Viking mission's krypton and xenon detections and measurements of noble gas isotope ratios in martian meteorites. However, the meteorite measurements reveal an impure mixture of atmospheric, mantle, and spallation contributions. The xenon and krypton isotopic measurements reported here include the complete set of stable isotopes, unmeasured by Viking. The new results generally agree with Mars meteorite measurements but also provide a unique opportunity to identify various non-atmospheric heavy noble gas components in the meteorites. Kr isotopic measurements define a solar-like atmospheric composition, but deviating from the solar wind pattern at ^{80}Kr and ^{82}Kr in a manner consistent with contributions originating from neutron capture in Br. The Xe measurements suggest an intriguing possibility that isotopes lighter than ^{132}Xe have been enriched to varying degrees by spallation and neutron capture products degassed to the atmosphere from the regolith, and a model is constructed to explore this possibility. Such a spallation component, however, is not apparent in atmospheric Xe trapped in the glassy phases of martian meteorites.

Keywords

Krypton; xenon; Mars atmosphere; Mars evolution; Mars Science Laboratory; Mars meteorites

1. Introduction

The noble gases are key indicators of planetary evolution. Krypton and xenon are especially useful with their large numbers of stable isotopes; six and nine respectively, making them ideal for tracking source reservoirs and for understanding the evolution of planetary interiors and atmospheres. Many of the isotopes are formed or fractionated by distinct mechanisms, so their enrichment or depletion can be informative with regard to source: ^{129}Xe is produced by decay of ^{129}I, a now extinct radioactive nuclide with a half-life of 15.7 Myr. Isotopes ^{131}Xe, ^{132}Xe, ^{134}Xe and ^{136}Xe are produced by actinide fission. Radiogenic ^{129}Xe and ^{136}Xe can be used (along with other noble gas isotopes) to test hypotheses for atmospheric formation and loss: their ^{129}I and ^{244}Pu parent species abundances at the time of Earth and Mars' formation are constrained by their radiogenic daughters in the atmospheres. Comparison of planetary interior values (trapped in mantle phases of igneous rocks) with atmospheric abundances and solar wind abundances can reveal how long ago ^{129}Xe and ^{136}Xe were degassed (Podosek and Ozima, 2000). Excess ^{129}Xe relative to ^{130}Xe in Mars' atmosphere relative to interior components supports the hypothesis that Mars degassed soon after planetary accretion, while fractionation of Xe isotopes in the martian atmosphere may indicate substantial loss of atmosphere in a very early hydrodynamic escape phase (Pepin, 1991, 2000).

Previous to MSL, what we knew about martian noble gases was based on the noble gas measurements of Viking (Owen and Biemann, 1976; Owen et al., 1976; Owen et al., 1977) and the analyses of meteorites ejected from Mars. These meteorites: shergottites (Treiman and Filiberto, 2015), nakhlites (Treiman, 2005), chassignites (Treiman et al., 2007), ALH84001 (Treiman, 1998) and the basaltic breccia NWA7034 (Agee et al.,

2013) are petrologically distinct from primitive chondritic meteorites, and the compositional similarity of gases trapped in their impact melt inclusions to Mars' atmospheric values is what identified them as martian (Bogard and Johnson, 1983; Pepin, 1985; Wiens and Pepin, 1988). But martian meteorites all contain more than one noble gas component, and measurements therefore return a composite of unfractionated or fractionated martian atmosphere, martian interior gases, fission and cosmogenic additions, and terrestrial contamination.

An elementally unfractionated martian atmospheric component was first found in shock melt inclusions in the shergottite EETA 79001 (Bogard and Johnson, 1983; Becker and Pepin, 1984; Wiens et al., 1986; Swindle et al., 1986), establishing the link between the SNC meteorites and Mars. The Xe composition was found to be isotopically distinct from all other known xenon reservoirs, especially in its high $^{129}Xe/^{132}Xe$ ratio and enhanced $^{134}Xe/^{132}Xe$ and $^{136}Xe/^{132}Xe$ ratios (Swindle et al., 1986). This atmospheric component was refined using a range of shock melts from four different shergottites, resulting in a recommended $^{129}Xe/^{132}Xe$ ratio of 2.60 ± 0.05 for Mars' atmosphere (Bogard and Garrison, 1998). Most recently, a martian brecciated meteorite (NWA7034, 'Black Beauty') (Agee et al., 2013) was shown to contain dominantly unfractionated martian atmosphere (Cartwright et al., 2014), providing evidence that this component is not unique to the shergottites. Elementally fractionated Martian atmospheric component(s) are found in the nakhlites and ALH84001 (Swindle, 2002) and the Martian interior component was first identified in the Chassigny meteorite (Ott, 1988).

Terrestrial air can introduce both unfractionated and fractionated contamination to meteorites, with the latter mimicking interior signals (Mohapatra et al., 2009) or completely masking martian signatures (Schwenzer et al., 2013). Disentangling those components is key to understanding processes such as planetary formation. It also provides insights into surface-atmosphere interaction and ejection history, but only at the precision with which the individual components are known and understood. Precise *in situ* measurements of Xe and Kr in Mars' atmosphere are not hampered by complications introduced by "contaminating" noble gases.

2. Experimental

Previously, we reported measurements of the stable isotopes of argon ($^{40}Ar/^{36}Ar = 1.9 \pm 0.3 \times 10^3$ and $^{36}Ar/^{38}Ar = 4.2 \pm 0.1$ (Atreya et al., 2013; Mahaffy et al., 2013). The $^{40}Ar/^{36}Ar$ ratio used dynamic mass spectrometry to directly measure these masses. To obtain the ratio of ^{36}Ar to ^{38}Ar, it was necessary to develop a semi-static enrichment experiment to reach sufficiently high signal-to-noise (S/N) and background contrast for measurement of ^{38}Ar, the least-abundant Ar isotope (Atreya et al., 2013). However, while semi-static experiments provided moderate S/N and low enough background contrast to also enable Kr isotope measurements, they were unable to enrich the Xe signals to the extent necessary for precise isotopic measurement. That required development of a fully static mass spectrometry experiment (Table 1).

2.1 Static Mass Spectrometry

The relevant components of the SAM suite are described in Mahaffy et al. (2012). Gas is ingested, flowing through both zeolite (Linde 13x) and magnesium sulfate chemical scrubbers, effectively removing >95% of the CO_2 and H_2O, and weakly adsorbing all other active gases. The post-scrubber gas mix is enriched in N_2, Ar, Kr, and Xe, which then flows over a cooled hydrocarbon (HC) trap to efficiently trap out Xe, allowing other gases to pass. The HC trap consists of three adsorbents in series, Tenax® TA, silica beads, and carbosieve®. The approach and scripting were validated in the SAM high fidelity test bed at Goddard Space Flight Center.

The tunable laser spectrometer (TLS), which has been evacuated prior to atmospheric ingestion, is used as a storage volume so that gases not trapped out on the HC trap, particularly Kr, are collected here for later analysis.

The enrichment flows gas over the scrubbers and trap for 5400 seconds, after which the HC trap and TLS are closed off from the rest of the SAM manifolds. The manifolds are evacuated, and the scrubbers activated to clean them of adsorbed gas.

Xe-enriched gas collected on the trap is slowly released into the quadrupole mass spectrometer (QMS) in a semi-static scanning mode, where the conductance out to the pump is throttled to increase the S/N in the MS. Once the majority of the gas has been released into the manifold, the valve to the pump is closed, and the remaining gas is scanned in fully static mode. The low abundance of Xe allows fully static mode without increasing the pressure inside the mass spectrometer to a saturated level. The masses of interest (the nine stable Xe isotopes) are scanned. Once analysis of Xe is complete, the manifolds and MS are evacuated prior to releasing the Kr-enriched gas from the TLS. The QMS is returned to semi-static mode for analysis of Kr; static mode being too risky because of the high Ar partial pressure in the gas. Because Kr and Xe cannot be scanned at the same time in this method a direct measurement of the $^{84}Kr/^{132}Xe$ elemental ratio could not be obtained, nor could $^{84}Kr/^{36}Ar$ since the enrichment of ^{36}Ar saturates the detector.

2.2 Data processing.

Experimental Kr and Xe data were corrected for detector dead time, mass discrimination (Appendix A1), quadrupole mass spectrometer (QMS) tuning effects, and instrument background, as discussed in Franz et al. (2014). Because the background as well as analytic signal grew with time during the semi-static and static QMS modes utilized for Kr and Xe measurements, background models were based on tracer *m/z* representative of the instrument background. For Kr, a tracer of *m/z* 12 was used in experiment ID #25111 and *m/z* 79 in ID #25269. For Xe, *m/z* 127 was used as the tracer in both ID #25253 and ID #25269. The background model is implemented by scaling the trend exhibited by the tracer *m/z* based on the relative proportions of the analyte and tracer *m/z* during the background region prior to introduction of Xe or Kr gas to the manifold. Uncertainties in the background model were computed from the difference in isotope ratios derived with the nominal background model as described above and an alternate model. For Kr, the alternate background model used a tracer of *m/z* 55 in ID #25111 and *m/z* 63 in ID #25269. For Xe, the alternate background model for both ID #25253 and ID #25269 used a constant value at each relevant *m/z,* acquired before the Xe analysis region.

3. Results and Discussion

The number N of individually measured and corrected isotope ratios, their standard deviation and standard error of their mean (s.e.m.), and assessment of total error are set out in Tables 2 and 3 for all Xe and Kr analyses. A total of ~5000 individual ratios were included in the analyzed regions of the four experiments. Graphical displays of measurements vs. time, selected to include data sets for both low and high abundance Xe and Kr isotopes, are shown in Appendix A4. Tabulations of all Kr and Xe isotope ratio data used in the analyses, corrected for backgrounds, peak shapes and mass discriminations, are contained in Appendix A7.

The SAM isotopic compositions reported here for Xe and Kr in Mars' atmosphere are averages of results obtained in the repeated experiments, #25253 and #25269 for Xe and #25111 and #25269 for Kr. These were calculated in two ways from the separate experiment results: (a) unweighted averages with s.e.m. errors given by their standard deviation/$\sqrt{2}$; or (b) $1/\sigma_j^2$-weighted averages where σ_j is the ± 1 sigma error in each of the two experiments. The first ignores errors in the individual experiement measurements, the second takes them explicitly into account. Final Xe and Kr compositions calculated using both averaging protocols are listed in Tables 2 and 3.

3.1 Xenon.

Comparisons of the experiment ID#25253 and ID#25269 averages in Table 2 show satisfactory reproducibility of the separately measured isotopic compositions. Differences between the individual isotope ratio sets (e.g. $[^{124}Xe/^{132}Xe \pm \sigma]_{25269}$ - $[^{124}Xe/^{132}Xe \pm \sigma]_{25253}$) are all <60% of the errors in the differences; across the Xe spectrum they average

~30%. This agreement is reflected in the close correspondence of the unweighted and $1/\sigma^2$-weighted averages in Table 2, within —and for isotope masses > 126 well within— their associated uncertainties. In this case it seems appropriate to select $1/\sigma^2$-weighted averaging: it biases results toward the more precise experiment #25269 data, and also generates more conservative errors than unweighted averaging.

Atmospheric Xe isotope ratios relative to ^{132}Xe generated from the SAM data in this way are plotted in Fig. 1 relative to the composition of Genesis SW-Xe (Meshik et al., 2015), together with measurements listed in Table 2 on shergottite glasses from EETA79001 (Swindle et al., 1986) and EETA79001 + Zagami (Mathew et al., 1998). Error bars are shown where they exceed the symbol sizes. Effects of adopting unweighted instead of $1/\sigma^2$-weighted averaging are indicated by the white squares at ^{124}Xe and ^{126}Xe. The two averaging protocols yield statistically indistinguishable results at these minor isotopes, and in fact for all isotopes.

The solid curve in Fig. 1 represents Meshik et al's SW-Xe mass-fractionated in hydrodynamic escape (Appendix A6) to the degree required for best fit the EETA79001 and EETA + Zagami measurements. Correspondence of the curve with the meteorite data is striking. The SAM atmospheric measurements for isotopes heavier than ^{126}Xe generally follow the same pattern. Averaged δ^{128}Xe and δ^{130}Xe-δ^{136}Xe ratios in Fig. 1 agree with the fractionation curve, and therefore with the meteorites, to within ~ 25‰ or less. These direct *in situ* measurements support the conclusion from the meteorite data that the base composition of atmospheric Xe on Mars, except for the large radiogenic

^{129}Xe contribution, is fractionated solar Xe (Pepin, 2000). This conclusion is reinforced by the observation that Mars' interior (i.e., mantle) Xe is very similar to SW-Xe (Jakosky and Jones 1997; Swindle and Jones, 1997; Ott, 1998; Swindle, 2002).

However significant offsets of the nonradiogenic atmospheric ratios from the curve are evident, large for $\delta^{124}Xe$ and $\delta^{126}Xe$, smaller for $\delta^{128}Xe$ and $\delta^{131}Xe$ but still up to > 5x their mean errors above the average meteorite ratios. The origins of these nonradiogenic excesses are presently not understood. There are no identified analytic mass interferences at these isotopes that could account for them, from products found in SAM that could be contaminants in the gas processing manifold or mass spectrometer. We have calculated the potential effect of masses that could be associated with the degradation of the SAM derivatisation reagent N-Methyl-N-(tert-butyldimethylsilyl)-trifluoroacetamide (MTBSTFA), vapors of which were previously reported to have been released and detected as a hydrocarbon background in SAM solid sample analyses (Glavin et al., 2013) and find that such a background subtraction would still be insufficient to account for the elevated ^{124}Xe and ^{126}Xe (Appendix A3). However small background signals are indeed seen at these masses, whatever their origin. These were incorporated into the background model and subtracted to yield corrected isotope ratios. It is interesting to note that Viking also detected high abundances at the trace masses 124 and 126, though they were unable to report them quantitatively (Owen et al., 1977). Although attributed to hydrocarbon contamination, they could alternatively suggest the interesting possibility that these, in part, were the first hint of elevated light masses of Xe in the martian atmosphere.

Another possible explanation for elevation of the light Xe isotope ratios above the SW fractionation curve, discussed in Sec. 3.3.1, is the presence of spallogenic and neutron-capture Xe produced by galactic cosmic ray (GCR) irradiation of target elements in soil and rocks on or near the martian surface and released over time into the atmosphere. Such degassing of a regolith product generated from neutron-irradiated Br is a likely explanation for the presence of excess ^{80,82}Kr in the atmospheric Kr trapped in the shergottite glasses (Sec.3.2).

3.2 Krypton.

SAM measurements at m/z = 78 were compromised by a large unresolved interference, most likely due to known benzene or dichloropropane fragmentation contaminants in the gas processing system. ^{78}Kr/^{84}Kr ratios are therefore not reported. Some of the other isotope ratios measured in the two Kr experiments show more scatter than is present in the Xe experiments. For ^{80}Kr/^{84}Kr and ^{86}Kr/^{84}Kr in particular, differences in ratio averages exceed the errors in their differences by a factor of ~2 (Table 3). It is possible that dissimilar experimental techniques, including different gas pathways and scanning sequences for experiments #25111 and #25269, could have played a role. Modification of the method for Kr isotope measurements in #25269 was necessary in order to achieve the static mode for Xe isotope measurements, although the Kr was measured in semi-static mode (sec. 2.1). There is no evidence, however, that either of these analyses by itself is the better representative of atmospheric Kr composition. In this situation unweighted averaging of the data sets is the more conservative choice since the s.e.m. values overlap both of the individual experiment ID averages while errors associated with $1/\sigma^2$-weighted averages do not (Table 3). However, the uncertainty shown in the table for averaged $^{83}Kr/^{84}Kr$ is unrealistically small (~ ±1.5‰) compared to other isotopes. It likely reflects fortuitous agreement of this ratio in the two experiments. An alternative and perhaps overly conservative estimate is the average uncertainty of ~ ±18‰ in the separate experiment measurements (Table 3).

Figure 2 shows the averaged data from the SAM experiments compared to the solar wind (Meshik et al., 2014) and meteorite compositions. The SAM Kr isotopic distribution agrees with the SW composition within ±1σ uncertainty at ^{86}Kr, and also at ^{83}Kr if the plotted alternate error suggested above is adopted, but show substantial enrichments above the SW trend for the light isotopes ^{80}Kr and ^{82}Kr. Elevations above SW-Kr at these two isotopes, although at considerably lower levels, are also observed in Kr trapped in shock glasses from the EETA79001 shergottite (Fig. 2) and are thought to result from neutron capture in Br via $^{79,81}Br(n,\gamma\beta^-)^{80,82}Kr$ (Becker and Pepin, 1984; Swindle et al., 1986; Rao et al., 2002). Moreover, there is evidence that these excesses originated on Mars, and are not due to capture of neutrons generated by in-space GCR irradiation during meteorite transits from Mars to Earth (Swindle et al., 1986; Rao et al., 2002).

The relative magnitudes of the $^{80,\,82}Kr$ excesses measured by SAM support the capture hypothesis. If the ^{80}Kr elevations are due solely to $^{79}Br(n,\gamma\beta^-)^{80}Kr$ reactions, one can calculate from the ^{79}Br and ^{81}Br neutron capture cross sections what the corresponding enhancement at ^{82}Kr from $^{81}Br(n,\beta^-)^{82}Kr$ would be. Sums of resonance integrals for high, epithermal, and thermal energy neutron capture in ^{79,81}Br (Dorval et al., 2008) yield an ^{80}Kr/^{82}Kr production ratio of 2.58 ± 0.25, indistinguishable from the ~2.5 ratio that accounts for ^{80}Kr and ^{82}Kr excesses in large chondritic meteorites (Marti et al., 1966). Application of Dorval et al.'s production ratio to the excesses above solar of ^{80,82}Kr observed in both the SAM and meteorite data (Table 3, Fig. 2) yields the corrected ^{80,82}Kr/^{84}Kr ratios indicated by the diamond symbols in Fig. 2. Corrected ^{80}Kr/^{84}Kr is solar ($\delta = 0$) by assumption. The n-corrected SAM ^{82}Kr/^{84}Kr ratio falls at δ = -6‰, a nominal reduction of ~60‰ from the measured value. The attached error bar includes the ^{82}Kr/^{84}Kr measurement error plus augmentations due to uncertainties in measured ^{80}Kr/^{84}Kr and the ^{80}Kr/^{82}Kr production ratio.

It is evident that the ^{82}Kr/^{84}Kr ratios, without their n-capture components, are close to solar for both the meteorite measurements and those reported here for the atmosphere if the corrected ^{80}Kr/^{84}Kr ratios are likewise solar. This strengthens the view that Mars' base atmospheric Kr composition is in fact solar, overlain by neutron capture components at ^{80,82}Kr. An unexplained puzzle is why the meteorite glasses, which purport to sample the recent atmosphere, display much smaller n-capture excesses than those in the present-day atmosphere (Fig. 2).

Garrison and Bogard (1998) propose that enrichments of $^{80-83}$Kr/^{84}Kr and a depletion of ^{86}Kr/^{84}Kr relative to the solar composition, observed in one sample of EETA 79001 impact glass, signal the presence of mass-fractionated solar Kr in which an ^{80}Kr excess is absent or minor. However, both the meteorite and direct atmospheric measurements in

Fig. 2, including those of Swindle et al. (1986) which are viewed as the most precise for the meteorites, show no evidence for such fractionation.

3.3 Regolith-derived spallation and neutron-capture Xe and Kr in the martian atmosphere?

3.3.1 Xenon.

Excesses in δ^{124}Xe and δ^{126}Xe are often signatures of spallation Xe components. Their presence in the SAM data suggests that the martian atmosphere may contain spallogenic and neutron capture products generated in and outgassed from the regolith (Rao et al., 2002). Assuming that atmospheric spallation and $(n,\gamma\beta^{-})$ components are actually present in the atmosphere, corrections to the SAM measurements were calculated using the following parameters:

3.3.1.1. *A REE/Ba wt.% ratio of 0.54.* GCR spallations of Ba and the rare earth elements (REE) are the dominant contributors to spallogenic Xe. Spallation Xe production rates for these elements are given in Hohenberg et al. (1978). They are calculated using a ratio of 6.9 for REE abundances summed from Ce to Er, relative to La abundance. Of interest for this model is Hohenberg et al.'s (Ce + Pr)/La ratio of 3.0. In the 6 SNC meteorites for which data exist in the Lodders (1998) compilation, this ratio is 3.0 ± 0.5. Although there are insufficient SNC abundance data to enable similar comparisons for most of the heavier REEs, this agreement suggests that they are also likely to be approximately compatible with Hohenberg et al.'s REE distributions. The SNC La/Ba ratio is 0.069 ± 10% (Lodders, 1998), and therefore "La"/Ba, with "La" including all the REE targets, is probably reasonably close to 0.069 x (1 + 6.9) = 0.54. REE concentrations on Mars are unknown. The REE/Ba ratio of 0.54 that arguably characterizes the SNC meteorites is taken as proxy for the martian regolith.

Spallation production rates used in this modeling are from (Hohenberg et al., 1978), calculated for a La/Ba ratio set to 0.069 and an adjustable Ba abundance (Sec. 3.3.1.3). They are integrated over a regolith depth of ~500 g/cm^2. The resulting spallation composition is listed in Table 4. To account for the present atmospheric overburden of ~17 g/cm^2 the regolith surface was repositioned to 17 g/cm^2 and production rates were integrated from this depth to 500 g/cm^2. No attempt was made to calculate production rate variations due to different —and unknown— atmospheric densities that could have occurred over the past 3700 Ma.

3.3.1.2. *A 43% regolith degassing efficiency.* Martian Br is taken to be 36 ppm, about midway in the concentration range measured by Pathfinder (Gellert et al., 2004) and Curiosity (Blake et al., 2013). Combined with modeling of neutron capture by ^{79}Br in the regolith (Rao et al., 2002) the ^{80}Kr excess measured by SAM (Fig. 2) requires 43% degassing of the regolith inventory produced over 3700 Ma by GCR-generated neutrons. This 43% release is assumed to apply to spallogenic and $(n,\gamma\beta^-)$ Xe products as well.

3.3.1.3. *With these choices, the Ba concentration in the martian regolith is a free parameter in the model.* Results of applying it to the static experiment #25269 Xe measurements, the more precise of the two data sets, are shown in Fig. 3. Barium abundance was adjusted until spallation-corrected δ^{124}Xe and δ^{126}Xe were equally spaced on either side of the fractionated SW curve, both within ~1σ error of the curve or less (Fig. 4). Required Ba concentration in this baseline model is 602 ppm. Other fits of corrected δ^{124}Xe and δ^{126}Xe to fractionated SW are possible; for example, error-weighting their positions relative to the curve, which would move δ^{124}Xe closer and δ^{126}Xe further away. But this has only a minor (<10%) effect on required Ba.

Effects on isotope ratios of subtracting calculated spallation and neutron capture components are set out numerically in Table 4 and plotted in Fig. 3 and, at higher resolution, in Fig. 4. Essentially all of the δ^{128}Xe excess is removed by spallation correction. Additional production of ^{128}Xe by ^{127}I(n,γβ^{-})^{128}Xe capture is probably minor. Estimates for iodine in the martian regolith range from ~100 ppb in three non-Antarctic, presumably uncontaminated SNCs (Lodders, 1998) to ~500 ppb with large uncertainty (Rao et al., 2002). Correction for production from iodine at the 100 ppb level is negligible (~1‰), and only ~10‰ even with 10x this abundance (Table 4). Spallation corrections to measured δ^{130}Xe and δ^{131}Xe are small (< 5‰). Most of the δ^{131}Xe excess is attributable to n-capture in Ba, but the ^{130}Ba(n,γβ^{-})^{131}Xe contribution is uncertain because the production rates given by Rao et al. (2002) and estimated from Hohenberg et al. (1978) differ by a factor of ~20, due primarily to a ~6-fold difference in adopted capture cross sections. Using the log average of the two ^{130}Ba(n,γβ^{-})^{131}Xe production rates —1.9 x 10^{15} atoms/s for Ba = 602 ppm in the baseline model— corrects δ^{131}Xe to within 10‰ of the fractionation curve, but with the large uncertainties shown in Table 4 and Fig. 3. Other isotope ratios (δ^{134}Xe, δ^{136}Xe, and ^{129}Xe/^{132}Xe) are essentially unchanged by spallation subtraction. Fig. 4 demonstrates that correction of the measured ID #25269 isotope ratios for the assumed presence of atmospheric spallation and (n,$\gamma\beta^-$) products leads to notable agreement with the fractionated SW and shergottite glass compositions. All corrected isotope ratios fall within error in the ±10‰ band around the fractionated SW reference composition, and only δ^{134}Xe is >1σ away from the reference.

The 602 ppm Ba content obtained for the baseline model is sensitive to adopted values of a number of parameters: (a) the ^{132}Xe atmospheric volume mixing ratio (VMR), not measured directly by SAM (Sec. 2.1) but derived from the measured ^{36}Ar VMR in Mars' atmosphere (Atreya et al., 2013; Mahaffy et al., 2013) and an estimate of ^{132}Xe/^{36}Ar from the shergottite glasses (Garrison and Bogard, 1998); (b) the La/Ba ratio in the martian regolith (Sec. 3.3.1.1); and (c) the regolith Br abundance which sets the regolith outgassing efficiency (Sec. 3.3.1.2). The latter has the most severe impact on Ba requirements. As regolith Br is varied over its most likely range of ~20 – 60 ppm (Blake et al., 2013; Gellert et al., 2004) with corresponding changes in regolith degassing efficiencies from 76% to 26% respectively, the Ba concentrations needed to replicate Figs. 3 and 4 range from 340 to 1020 ppm. Variations in any of these parameters produce proportional changes in required Ba, and so one cannot specify a single regolith Ba content that uniquely generates Figs. 3 and 4. However the model is resilient to parameter variations in the sense that a particular Ba value can always be found that reproduces the corrected composition in the figures. Varying these parameters within their probable uncertainty ranges leads to a spread in required Ba of ~200 to 1000 ppm.

3.3.1.4. *Barium.* Barium in martian soils and rocks has been measured by Curiosity's ChemCam LIBS instrument. Estimates range from a few 10's of ppm in sand and soil up to ~1640 ppm in a trachyte rock (Ollila et al., 2014; Payré et al., 2016); the majority of the measurements fall between ~100 and 500 ppm (Payré et al., 2016). The Ba concentration of~600 ppm in the baseline spallation model is significantly above their average. However, the ~200-1000 ppm spread in required Ba concentrations generated by variations in modeling parameters falls with the range of LIBS measurements reported by Payré et al.

Within its uncertainties, the Ba content of the martian regolith required by the model may be compared to the ~250 ppm estimate for Earth's bulk crust (McLennan, 2001; Payré et al., 2016) and ~350 ppm in ocean island basalts (OIB) (Sun and McDonough, 1989). The REE/Ba ratio of 0.54 adopted for Mars is close to Sun and McDonough's OIB value of ~0.56 and intermediate between ~0.34 in Earth's bulk continental crust (McLennan, 2001) and ~1.2 in oceanic crust (White and Klein, 2014), consistent with the more mafic nature of the martian surface compared to the terrestrial continental crust.

3.3.1.5. *Comparison with Xe trapped in shergottite glasses.* This spallation scenario is potentially capable of accounting for observed excesses in the SAM Xe data at nonradiogenic isotopes lighter than ^{132}Xe. It conflicts, however, with evidence that shock glasses in shergottites record the composition of the martian atmosphere. Xe trapped in glassy phases of EETA79001 (Swindle et al., 1986) and EETA79001 + Zagami (Mathew et al., 1998), plotted in Fig. 1, shows no evidence for the presence of atmospheric spallation or neutron capture Xe. These meteorites do display spallogenic enrichments in the light Xe isotopes, particularly in Zagami with its long exposure age, but these are consistent with production in space by GCR spallation during post-ejection transit from Mars to Earth (Swindle et al., 1986; Mathew et al., 1998). When these in situ spallation products are subtracted, δ^{124}Xe, δ^{126}Xe, and δ^{128}X ratios in the glasses fall close to the SW fractionation curve (Fig. 1) with no evident way to accommodate additional atmospheric spallation or $(n,\gamma\beta^-)$ components.

This could be a telling argument against the spallation hypothesis if the light isotope enhancements recorded by SAM could be shown to be attributable to hydrocarbon interferences, but no plausible candidates among species known to be present in the QMS analytic system have been identified (Appendix A3.1). The alternative to instrumental interferences, where the SAM light isotope signatures are taken to be true measures of atmospheric composition, would seem to require a specific degassing history for the martian regolith in which the bulk of spallation Xe products was released after the shergottite glasses had acquired their trapped atmosphere. However, there is relatively strong evidence that ^{80,82}Kr from neutron capture in regolith Br *was* degassed to the atmosphere and incorporated into the glasses (Sec. 3.2). At the moment neither of these potential explanations, either SAM hydrocarbon interferences or an arbitrarily constructed spallation degassing scenario, is particularly robust.

3.3.2. Atmospheric fission Xe on Mars?

Mars' atmosphere is notable for the large ^{129}Xe excess displayed by the SAM and shergottite glass measurements in Figs. 1 and 3, yet in none of these data sets are there discernable elevations of heavy isotope ratios that would signal the existence of a ^{244}Pu fission Xe component expected to accompany outgassed radiogenic ^{129}Xe (Swindle and Jones, 1997). Models suggesting that Pu-Xe is actually present but concealed, and their status from the perspective of the meteorite and SAM data in Tables 2 and 4, are discussed in Appendix A5.

3.3.3 Krypton.

The elevated atmospheric ^{80,82}Kr/^{84}Kr ratios measured by SAM (Sec. 3.2) appear to be consistent with addition of a Kr component generated in the regolith by neutron capture in Br. One would expect that release of these products into the atmosphere would be accompanied by degassing of Kr produced by GCR spallation of Rb, Sr, and other target elements. However, unlike the case for the light Xe isotopes, addition of spallogenic Kr has only a minimal and undetectable effect on measured Kr isotopic abundances. Average regolith Rb (65 ppm) and Sr (225 ppm) concentrations are reported by (Payré et al., 2016) and estimates of Y/Sr (~0.74) and Zr/Sr (~0.37) by (Clark et al., 1976). Using elemental production rates from these elements (Hohenberg et al., 1978) and the 43% degassing efficiency of regolith inventories required by the SAM ^{80}Kr excess and the selected martian Br concentration of 36 ppm (Sec. 3.3.1.2), calculated spallation contributions elevate ^{80}Kr by only ~2‰ and by <1‰ at the heavier isotopes.

4. Conclusions

SAM measurements of martian atmospheric Kr and Xe provide an in-situ benchmark for the SNC meteorite values. We see enrichments above the SNC isotopic values, particularly in the lighter isotopes of both Kr and Xe. What remains unclear, in particular for Xe, are the source(s) of the excesses. Either analytic mass interferences or the presence of atmospheric spallation and neutron capture components could cause such effects in Xe. The first of these possibilities seems doubtful since interfering species of sufficient magnitude appear to be absent in the SAM analytic system. The second is capable of explaining Xe isotope excesses relative to the fractionated SW composition, but conflicts with the observation that such components are not recorded in atmospheric Xe trapped in the shergottite glassy phases.

The elevated light isotopes in Kr (Fig. 2) are consistent with neutron capture in regolith bromine. The SAM measurements lend support to the proposal that Kr (and Xe) from neutron capture has been produced in the regolith and released into the atmosphere over time (Rao et al., 2002).

Measured δ^{134}Xe and δ^{136}Xe values are subject to neither resolvable spallation corrections or plausible mass interferences. SAM averages at these isotopes, and at δ^{130}Xe where a spallation contribution is minor, differ from the corresponding meteorite averages by <12‰ (Fig. 1). This strongly suggests that the base composition of Mars' atmospheric Xe follows the SW fractionation curve defined by the meteorite data. An assumed presence of spallation and $(n,\gamma\beta^-)$ Xe in the atmosphere can quantitatively account for elevations above the curve for the remaining nonradiogenic isotopes (Fig. 4).

The new SAM Xe data reinforce an old and enigmatic problem related to martian actinide chemistry and degassing history. Decay products of the extinct radionuclides ^{129}I and ^{244}Pu are both present in Earth's atmosphere (Pepin, 2000), but on Mars only one of these, a large excess of radiogenic ^{129}Xe, is apparent. This mystery has driven modeling attempts to argue that Xe from fission of ^{244}Pu actually is present in Mars' atmosphere but is fortuitously concealed from observation. Evaluation of such models in the context of the SAM and meteorite Xe data reported here suggests they are only marginally viable and in any case allow at most a minor contribution of Pu-Xe to the atmosphere (Appendix A5). Its near absence likely points to a very specific outgassing history for Mars, one in which ^{129}Xe from short-lived ^{129}I was released in early degassing but fission Xe from longer-lived ^{244}Pu is still sequestered within the planet.

It appears from the SAM Xe and Kr measurements that plausible arguments can be made for the presence of spallation and neutron capture products in the contemporary martian atmosphere. There are implications in this observation for understanding the breadth of regolith degassing by impact and other thermal pulses, and perhaps for the age of trapped atmosphere components in martian meteorites on the basis of accumulating n-capture and spallogenic contributions to the krypton and xenon inventories.

Acknowledgements

Special thanks to Richard Becker for helpful discussion regarding the data analysis. We are indebted to G. Avice and two anonymous reviewers for comments that greatly improved the manuscript. This work was funded by NASA's Mars Science Laboratory mission.

References

Agee, C.B., Wilson, N.V., McCubbin, F.M., Ziegler, K., Polyak, V.J., Sharp, Z.D., Asmerom, Y., Nunn, M.H., Shaheen, R., Thiemens, M.H., 2013. Unique meteorite from early Amazonian Mars: Water-rich basaltic breccia Northwest Africa 7034. Science 339, 780-785.

Atreya, S.K., Trainer, M.G., Franz, H.B., Wong, M.H., Manning, H.L., Malespin, C.A., Mahaffy, P.R., Conrad, P.G., Brunner, A.E., Leshin, L.A., 2013. Primordial argon isotope fractionation in the atmosphere of Mars measured by the SAM instrument on Curiosity and implications for atmospheric loss. Geophysical research letters 40, 5605-5609.

Becker, R.H., Pepin, R.O., 1984. The case for a Martian origin of the shergottites: Nitrogen and noble gases in EETA 79001. Earth and Planetary Science Letters 69, 225-242.

Blake, D.F., Morris, R., Kocurek, G., Morrison, S., Downs, R., Bish, D., Ming, D., Edgett, K., Rubin, D., Goetz, W., 2013. Curiosity at Gale crater, Mars: Characterization and analysis of the Rocknest sand shadow. Science 341, 1239505.

Bogard, D.D., Garrison, D.H., 1998. Relative abundances of argon, krypton, and xenon in the Martian atmosphere as measured in Martian meteorites. Geochimica et Cosmochimica Acta 62, 1829-1835.

Bogard, D.D., Johnson, P., 1983. Martian gases in an Antarctic meteorite? Science 221, 651-654.

Cartwright, J., Ott, U., Herrmann, S., Agee, C., 2014. Modern atmospheric signatures in 4.4 Ga Martian meteorite NWA 7034. Earth and Planetary Science Letters 400, 77-87.

Clark, B.C., Baird, A., Rose, H.J., Toulmin, P., Keil, K., Castro, A.J., Kelliher, W.C., Rowe, C.D., Evans, P.H., 1976. Inorganic analyses of Martian surface samples at the Viking landing sites. Science 194, 1283-1288.

Dorval, E.L., Arribére, M.A., Guevara, S.R., 2008. Measurement of neutron capture resonance integrals on bromine isotopes. Nuclear Science and Engineering 159, 199-212.

Franz, H.B., Trainer, M.G., Wong, M.H., Manning, H.L., Stern, J.C., Mahaffy, P.R., Atreya, S.K., Benna, M., Conrad, P.G., Harpold, D.N., 2014. Analytical techniques for retrieval of atmospheric composition with the quadrupole mass spectrometer of the Sample Analysis at Mars instrument suite on Mars Science Laboratory. Planetary and Space Science 96, 99-113.

Garrison, D.H., Bogard, D.D., 1998. Isotopic composition of trapped and cosmogenic noble gases in several Martian meteorites. Meteoritics & Planetary Science 33, 721-736.

Gellert, R., Rieder, R., Anderson, R., Brückner, J., Clark, B., Dreibus, G., Economou, T., Klingelhöfer, G., Lugmair, G., Ming, D., 2004. Chemistry of rocks and soils in Gusev Crater from the Alpha Particle X-ray Spectrometer. Science 305, 829-832.

Glavin, D.P., Freissinet, C., Miller, K.E., Eigenbrode, J.L., Brunner, A.E., Buch, A., Sutter, B., Archer, P.D., Atreya, S.K., Brinckerhoff, W.B., 2013. Evidence for perchlorates and the origin of chlorinated hydrocarbons detected by SAM at the Rocknest aeolian deposit in Gale Crater. Journal of Geophysical Research: Planets 118, 1955-1973.

Hohenberg, C., Podosek, F., Shirck, J., Marti, K., Reedy, R., 1978. Comparisons between observed and predicted cosmogenic noble gases in lunar samples, 9th Lunar and Planetary Science Conference Proceedings, pp. 2311-2344.

Jakosky, B.M., Jones, J.H., 1997. The history of Martian volatiles. Reviews of Geophysics 35, 1-16.

Lodders, K., 1998. A survey of shergottite, nakhlite and chassigny meteorites whole-rock compositions. Meteoritics & Planetary Science 33, A183-A190.

Mahaffy, P.R., Webster, C.R., Atreya, S.K., Franz, H., Wong, M., Conrad, P.G., Harpold, D., Jones, J.H., Leshin, L.A., Manning, H., 2013. Abundance and isotopic composition of gases in the martian atmosphere from the Curiosity rover. Science 341, 263-266.

Mahaffy, P.R., Webster, C.R., Cabane, M., Conrad, P.G., Coll, P., Atreya, S.K., Arvey, R., Barciniak, M., Benna, M., Bleacher, L., 2012. The sample analysis at Mars investigation and instrument suite. Space Sci Rev 170, 401-478.

Marti, K., Eberhardt, P., Geiss, J., 1966. Spallation, fission, and neutron capture anomalies in meteoritic krypton and xenon. Zeitschrift für Naturforschung A 21, 398-426.

Mathew, K.J., Kim, J.S., Marti, K., 1998. Martian atmospheric and indigenous components of xenon and nitrogen in SNC meteorites. Meteoritics and Planetary Science 33, 655-664.

McLennan, S.M., 2001. Relationships between the trace element composition of sedimentary rocks and upper continental crust. Geochemistry, Geophysics, Geosystems 2.

Meshik, A., Hohenberg, C., Pravdivtseva, O., Burnett, D., 2014. Heavy noble gases in solar wind delivered by Genesis mission. Geochimica et Cosmochimica Acta 127, 326-347.

Meshik, A., Pravdivtseva, O., Hohenberg, C., Burnett, D., 2015. Refined Composition of Solar Wind Xenon Delivered by Genesis: Implication for Primitive Terrestrial Xenon, 46th Lunar and Planetary Science Conference, Abstract #2640.

Mohapatra, R.K., Schwenzer, S.P., Herrmann, S., Murty, S., Ott, U., Gilmour, J.D., 2009. Noble gases and nitrogen in Martian meteorites Dar al Gani 476, Sayh al Uhaymir 005 and Lewis Cliff 88516: EFA and extra neon. Geochimica et Cosmochimica Acta 73, 1505-1522.

Ollila, A.M., Newsom, H.E., Clark, B., Wiens, R.C., Cousin, A., Blank, J.G., Mangold, N., Sautter, V., Maurice, S., Clegg, S.M., 2014. Trace element geochemistry (Li, Ba, Sr, and Rb) using Curiosity's ChemCam: Early results for Gale crater from Bradbury Landing Site to Rocknest. Journal of Geophysical Research: Planets 119, 255-285.

Ott, U., 1988. Noble gases in SNC meteorites: Shergotty, Nakhla, Chassigny. Geochimica et Cosmochimica Acta 52, 1937-1948.

Owen, T., Biemann, K., 1976. Composition of the atmosphere at the surface of Mars: Detection of argon-36 and preliminary analysis. Science 193, 801-803.

Owen, T., Biemann, K., Rushneck, D., Biller, J., Howarth, D., LaFleur, A., 1976. The atmosphere of Mars: detection of krypton and xenon. Science 194, 1293-1295.

Owen, T., Biemann, K., Rushneck, D., Biller, J., Howarth, D., Lafleur, A., 1977. The composition of the atmosphere at the surface of Mars. Journal of Geophysical Research 82, 4635-4639.

Payré, V., Fabre, C., Cousin, A., Forni, O., Gasnault, O., Rapin, W., Meslin, P.Y., Sautter, V., Maurice, S., Wiens, R.C., Clegg, S., 2016 Trace elements in Gale Crater: Li, Sr, Rb and Ba abundances using ChemCam data, 47th Lunar and Planetary Science Conference, Abstract #1348.

Pepin, R.O., 1985. Evidence of Martian origins. Nature 317, 473-475.

Pepin, R.O., 1991. On the origin and early evolution of terrestrial planet atmospheres and meteoritic volatiles. Icarus 92, 2-79.

Pepin, R.O., 2000. On the isotopic composition of primordial xenon in terrestrial planet atmospheres, Space Sci. Rev. 92, 371-395.

Podosek, F.A., Ozima, M., 2000. The xenon age of the Earth. Origin of the Earth and Moon 1, 63-72.

Rao, M., Bogard, D., Nyquist, L., McKay, D., Masarik, J., 2002. Neutron capture isotopes in the Martian regolith and implications for Martian atmospheric noble gases. Icarus 156, 352-372.

Schwenzer, S., Greenwood, R., Kelley, S., Ott, U., Tindle, A., Haubold, R., Herrmann, S., Gibson, J., Anand, M., Hammond, S., 2013. Quantifying noble gas contamination during terrestrial alteration in Martian meteorites from Antarctica. Meteoritics & Planetary Science 48, 929-954.

Sun, S.-S., McDonough, W.F., 1989. Chemical and isotopic systematics of oceanic basalts: implications for mantle composition and processes. Geological Society, London, Special Publications 42, 313-345.

Swindle, T.D., Caffee, M.W., Hohenberg, C.M., 1986. Xenon and other noble gases in shergottites. Geochimica et Cosmochimica Acta 50, 1001-1015.

Swindle, T.D, Jones, J.H., 1997. The xenon isotopic composition of the primordial Martian atmosphere: contributions from solar and fission components. Journal of Geophysical Research: Planets 102, 1671-1678.

Swindle, T.D., 2002. Martian noble gases. Reviews in Mineralogy and Geochemistry 47, 171-190.

Treiman, A.H., 1998. The history of Allan Hills 84001 revised: Multiple shock events. Meteoritics & Planetary Science 33, 753-764.

Treiman, A.H., 2005. The nakhlite meteorites: Augite-rich igneous rocks from Mars. Chemie der Erde-Geochemistry 65, 203-270.

Treiman, A.H., Dyar, M.D., McCanta, M., Noble, S.K., Pieters, C.M., 2007. Martian dunite NWA 2737: Petrographic constraints on geological history, shock events, and olivine color. Journal of Geophysical Research: Planets (1991–2012) 112.

Treiman, A.H., Filiberto, J., 2015. Geochemical diversity of shergottite basalts: Mixing and fractionation, and their relation to Mars surface basalts. Meteoritics & Planetary Science 50, 632-648.

White, W.M., Klein, E.M., 2014. Composition of the Oceanic Crust, Treatise of Geochemistry, 2nd ed, pp. 457-496.

Wiens, R.C., Pepin, R.O., 1988. Laboratory shock emplacement of noble gases, nitrogen, and carbon dioxide into basalt, and implications for trapped gases in shergottite EETA 79001. Geochim. Cosmochim. Acta 52, 295-307.

Wiens, R.C., Becker, R.H., Pepin, R.O., 1986. The case for a Martian origin of the shergottites, II. Trapped and indigenous gas components in EETA 79001 glass. Earth and Planetary Science Letters 77, 149-158.

Figure captions

Figure 1. Martian meteorite, fractionated solar wind, and average SAM Xe data plotted as δ-values referenced to the solar wind (SW) composition, where $\delta^{M}Xe = 1000\,[(^{M}Xe/^{132}Xe)_{measured} / (^{M}Xe/^{132}Xe)_{SW} - 1]$ ‰. SW ratios from Meshik et al. (2015). SAM ratios are $1/\sigma_j^2$-weighted averages of the two expt ID Xe averages in Table 2, where σ_j is the ±1σ error in each (Sec. 3.1); $1/\sigma^2$-weighted error bars shown where exceeding symbol sizes. White squares at ^{124}Xe and ^{126}Xe are δ-values obtained by unweighted averaging of the two average expt ID ratios (Table 2). Differences between the heavier isotope δ-values for the two types of averaging are too small to be visible at the scale of the figure.

Figure 2. Martian meteorite and average SAM Kr data plotted as δ- values referenced to the SW composition, where δ^{M}Kr is defined as in Fig. 1 with Kr isotope ratios replacing Xe ratios in the δ equation. SW ratios from Meshik et al. (2014). SAM ratios from the unweighted averages of the two Kr averages in Table 3. Error bars for the SAM data reflect ±1σ standard errors of the means (s.e.m.) of the two data sets, except at ^{83}Kr where a more conservative error estimate is shown (Sec. 3.2, Table 3). Diamond symbols at M = 80 and 82 denote subtractions from measured ^{80,82}Kr/^{84}Kr ratios of isotopes produced by neutron capture in Br; details discussed in Sec. 3.2.

Figure 3. As in Fig. 1, but here for measured SAM Xe ratios and errors in expt ID #25269 alone. Corrections for hypothetical atmospheric spallation and n-capture ^{127}I(n,γβ^-)^{128}Xe and ^{130}Ba(n,γβ^-)^{131}Xe components (yellow squares) discussed in Sec. 3.3 and listed in Table 4. Upper and lower tips of the asymmetric error bar around δ^{131}Xe denote different corrections calculated for ^{130}Ba(n,γβ^-)^{131}Xe contributions using, respectively, the Hohenberg et al. (1978) and Rao et al. (2002) n-capture production rates.

Figure 4. expt ID #25269 Xe ratios corrected for spallation and (n,γβ^-) products (yellow squares) compared with fractionated solar Xe ratios. The expt ID #25269 and meteorite data are referenced here to the fractionated solar composition itself and differences are therefore illustrated at higher resolution than in Fig. 3. Discussion and data in Sec. 3.3.1 and Table 4. See Fig. 3 caption for discussion of asymmetric error at δ^{131}Xe.

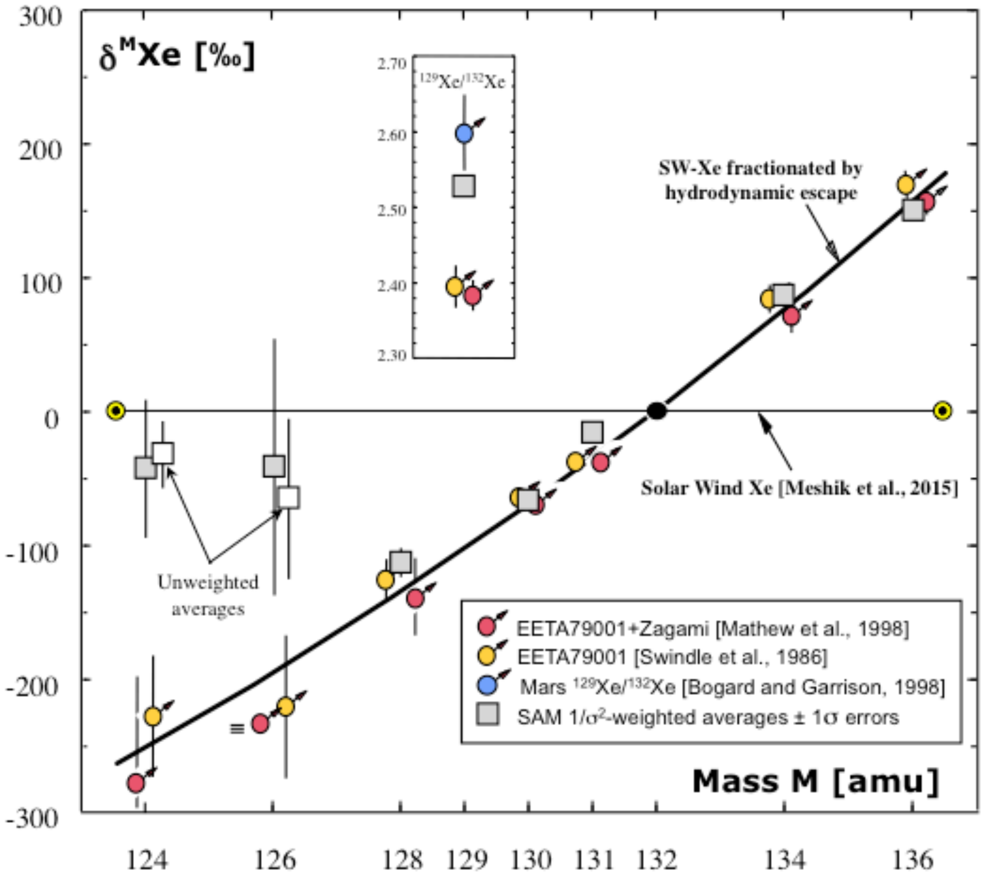

δ^M Xe [‰]
300
200
100
0
-100
-200
-300
124
126
128
129
130
131
132
134
136
Mass M [amu]
2.70
2.60
2.50
2.40
2.30
129Xe/132Xe
SW-Xe fractionated by hydrodynamic escape
Solar Wind Xe [Meshik et al., 2015]
Unweighted averages
EETA79001+Zagami [Mathew et al., 1998]
EETA79001 [Swindle et al., 1986]
Mars 129Xe/132Xe [Bogard and Garrison, 1998]
SAM 1/σ2-weighted averages ± 1σ errors

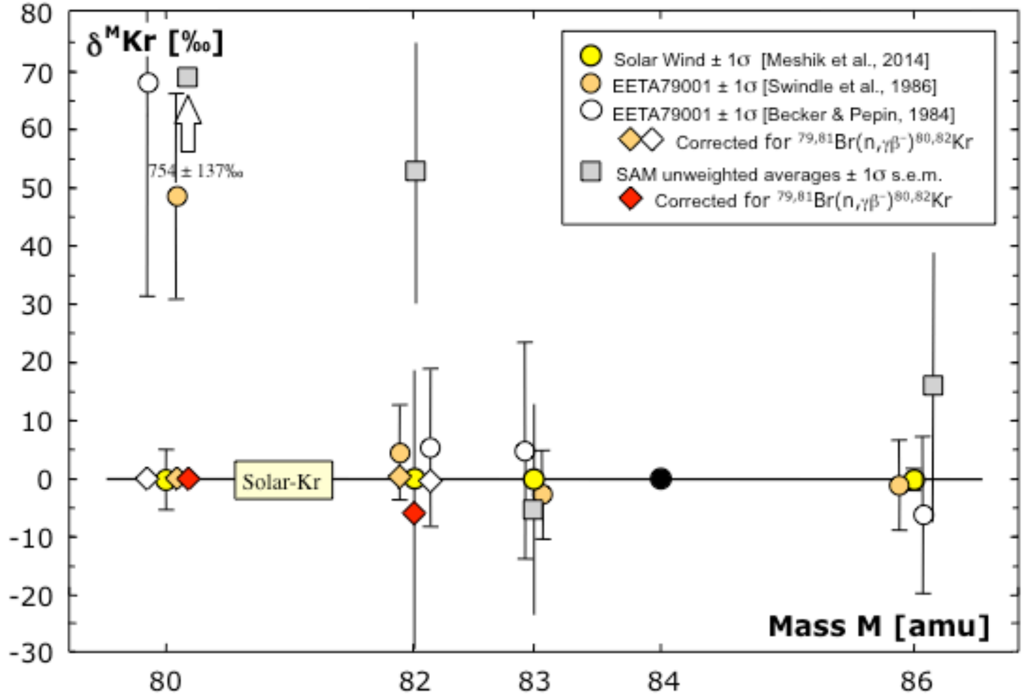

δ^{M}Kr [‰]
Solar Wind ± 1σ [Meshik et al., 2014]
EETA79001 ± 1σ [Swindle et al., 1986]
EETA79001 ± 1σ [Becker & Pepin, 1984]
Corrected for ^{79,81}Br(n,γβ$^-$)^{80,82}Kr
SAM unweighted averages ± 1σ s.e.m.
Corrected for ^{79,81}Br(n,γβ$^-$)^{80,82}Kr
754 ± 137‰
Solar-Kr
Mass M [amu]
80
70
60
50
40
30
20
10
0
-10
-20
-30
80
82
83
84
86

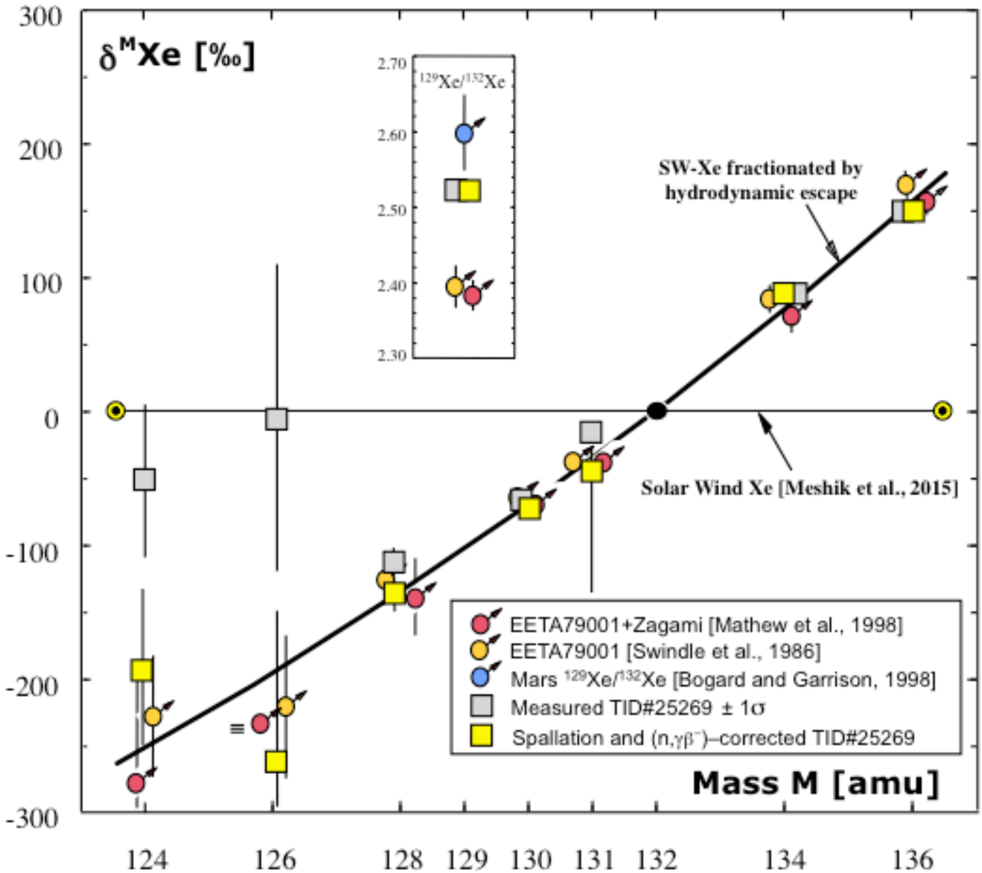

δ^M Xe [‰]
129Xe/132Xe
SW-Xe fractionated by hydrodynamic escape
Solar Wind Xe [Meshik et al., 2015]
EETA79001+Zagami [Mathew et al., 1998]
EETA79001 [Swindle et al., 1986]
Mars 129Xe/132Xe [Bogard and Garrison, 1998]
Measured TID#25269 ± 1σ
Spallation and (n,γβ⁻)–corrected TID#25269
Mass M [amu]

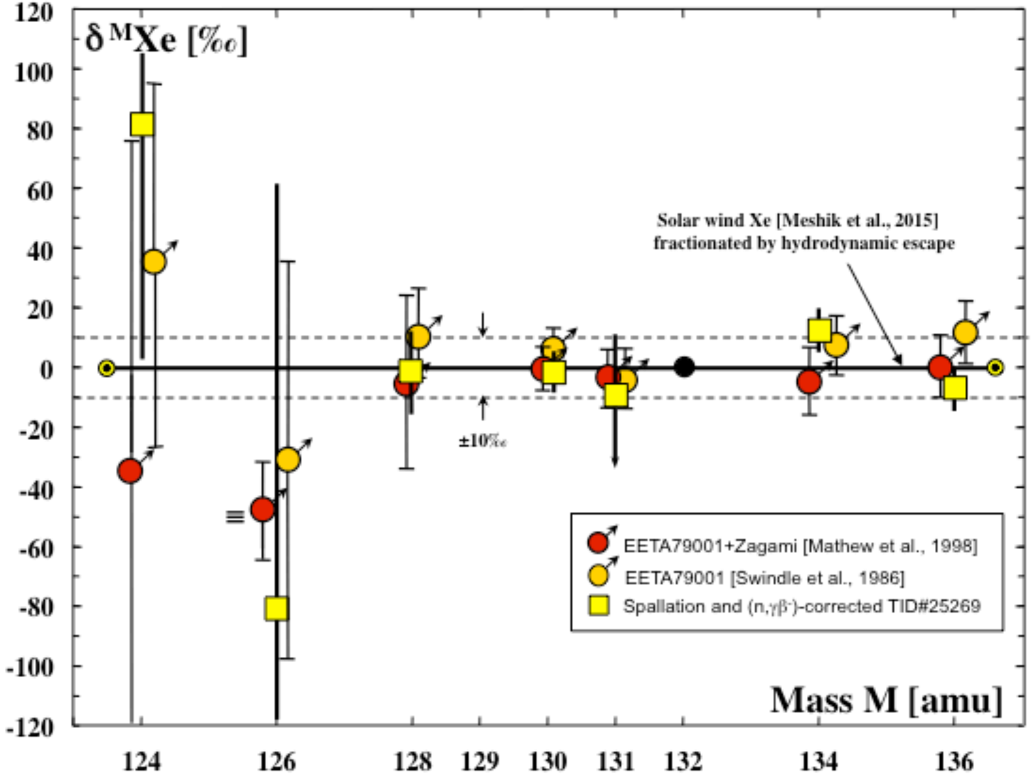

δ MXe [‰]
120
100
80
60
40
20
0
-20
-40
-60
-80
-100
-120
124
126
128
129
130
131
132
134
136
Mass M [amu]
±10‰
≡
Solar wind Xe [Meshik et al., 2015]
fractionated by hydrodynamic escape
EETA79001+Zagami [Mathew et al., 1998]
EETA79001 [Swindle et al., 1986]
Spallation and (n,γβ⁻)-corrected TID#25269

Table One: Semi-static and Static SAM Experiments on Mars

Semi-static Enrichment Mass Spectrometry

Experiment ID	Solar Longitude	Sol
25111 (Kr)	358	341
25269 (Kr)	336	976

Static Mass Spectrometry

25253 (Xe)	301	915
25269 (Xe)	336	976

Table 2: Xenon[(a)]

	124/132	126/132	128/132	129/132	130/132	131/132	134/132	136/132
ID#25253 (Static)	0.00483	0.00368	0.0757	2.5268	0.1542	0.8105	0.3982	0.3486
Standard deviation	0.00240	0.00303	0.0091	0.1042	0.0142	0.0377	0.0256	0.0261
No. of measured ratios N	74	74	74	74	74	74	74	74
s.e.m.	0.00028	0.00035	0.0011	0.0121	0.0017	0.0044	0.0030	0.0030
s.e.m. + bkg uncertainties[(b)]	0.00054	0.00073	0.0031	0.0668	0.0032	0.0089	0.0079	0.0125
δ wrt solar Xe [‰]	-13	-125	-101	1428	-64	-18	77	161
error [‰]	111	174	37	64	20	11	21	42
ID#25269 (Static)	0.00464	0.00418	0.0746	2.5221	0.1537	0.8125	0.4026	0.3451
Standard deviation	0.00230	0.00252	0.0081	0.0888	0.0132	0.0351	0.0247	0.0215
No. of measured ratios N	198	198	198	198	198	198	198	198
s.e.m.	0.00016	0.00018	0.0006	0.0063	0.0009	0.0025	0.0018	0.0015
s.e.m. + bkg uncertainties[(b)]	0.00028	0.00048	0.0008	0.0063	0.0010	0.0030	0.0027	0.0023
δ wrt solar Xe [‰]	-51	-5	-114	1423.9	-67.4	-15.9	88.6	149.3
error [‰]	58	115	10	6.5	6.2	4.0	7.5	7.8
Unweighted Average	0.00473	0.00393	0.07514	2.5245	0.15396	0.8115	0.4004	0.3468
s.e.m.	0.00009	0.00025	0.00055	0.0024	0.00026	0.0010	0.0022	0.0017
δ wrt solar Xe [‰]	-32	-65	-108	1426.2	-65.8	-17.1	82.7	155.0
s.e.m. [‰]	23	62	7	3.3	2.3	1.9	6.2	6.0
$1/\sigma^2$-weighted Average	0.00468	0.00403	0.07466	2.5221	0.15374	0.8123	0.4021	0.3452
error	0.00025	0.00040	0.00077	0.0063	0.00094	0.0029	0.0026	0.0022
δ wrt solar Xe [‰]	-43	-41	-113	1424.0	-67.1	-16.2	87.4	149.7
error [‰]	52	97	9	6.5	5.9	3.8	7.1	7.7
EETA 79001, Lith. C [1]	0.00378	0.00327	0.0735	2.394	0.1543	0.7930	0.4008	0.3514
error	0.00022	0.00022	0.0011	0.029	0.0010	0.0077	0.0039	0.0036
EETA 79001, Zagami [2]	0.00353	0.00322	0.0724	2.384	0.1532	0.7934	0.3959	0.3475
error	0.00040	≡ 0	0.0022	0.020	0.0010	0.0073	0.0042	0.0033
Genesis solar Xe [3]	0.00489	0.00420	0.08420	1.0405	0.16480	0.8256	0.36979	0.30030
error	0.00006	0.00007	0.00020	0.0010	0.00030	0.0012	0.00059	0.00049
Solar fractionation factor [4]	0.7470	0.8035	0.8643	0.8964	0.9297	0.9642	1.0757	1.1570
error[(c)]	0.0050	0.0040	0.0029	0.0022	0.0015	0.0008	0.0018	0.0038
Fractionated solar Xe	0.00365	0.00338	0.0728	0.9327	0.1532	0.7960	0.3978	0.3475
error	0.00005	0.00006	0.0003	0.0025	0.0004	0.0013	0.0009	0.0013
Fract. solar wrt solar [‰]	-253	-196	-135.7	-103.6	-70.3	-35.8	75.7	157.0
error [‰]	14	19	4.1	2.5	2.8	2.1	3.0	4.7

(a) ^{130}Xe/^{132}Xe ratios corrected for interference by ^{129}XeH hydride (Appendix A2). All ratio data in App. A7.
(b) Total error, including uncertainties in background (bkg) corrections. Error augmentations based on differences in isotope ratios yielded by the selected and alternate background subtraction models (Sec. 2.2).
(c) Estimated variance in fit to meteorite data.

Table 2 References: [1] Swindle et al., 1986 [2] Mathew et al., 1998 [3] Meshik et al., 2015 [4] Appendix A6

Table 3: Krypton

	80/84	82/84	83/84	86/84
ID#25111 (Semi-static)	0.0666	0.2209	0.2021	0.3129
Standard deviation	0.0316	0.0598	0.0521	0.0651
No. of measured ratios N	247	247	247	247
s.e.m.	0.0020	0.0038	0.0033	0.0041
s.e.m. + bkg uncertainties (a)	0.0021	0.0041	0.0033	0.0042
δ wrt solar Kr [‰]	617	75	-6	39
error [‰]	52	20	16	14
ID#25269 (Semi-static)	0.0779	0.2116	0.2025	0.2989
Standard deviation	0.0418	0.0657	0.0658	0.0810
No. of measured ratios N	432	432	432	432
s.e.m.	0.0020	0.0032	0.0032	0.0039
s.e.m. + bkg uncertainties (a)	0.0053	0.0080	0.0041	0.0057
δ wrt solar Kr [‰]	891	30	-4	-8
error [‰]	129	39	20	19
Unweighted Average	0.0723	0.2163	0.2023	0.3059
s.e.m.	0.0056	0.0047	0.0002	0.0070
δ wrt solar Kr [‰]	754	53	-5.4	16
s.e.m. [‰]	137	23	1.4 (b)	23
$1/\sigma^2$-weighted Average	0.0681	0.2190	0.2023	0.3075
error	0.0020	0.0036	0.0026	0.0033
δ wrt solar Kr [‰]	654	66	-6	21
error [‰]	48	18	13	11
EETA 79001, Lith. C [1]	0.0432	0.2063	0.2029	0.3009
error	0.0007	0.0017	0.0015	0.0023
EETA 79001, Lith. C [2]	0.0440	0.2065	0.2044	0.2993
error	0.0015	0.0028	0.0038	0.0039
Genesis solar Kr [3]	0.0412	0.2054	0.2034	0.3012
error	0.0002	0.0002	0.0002	0.0004

(a) Total error, including uncertainties in background (bkg) corrections. Error augmentations based on differences in isotope ratios yielded by the selected and alternate background subtraction models (Sec. 2.2). Standard deviation and s.e.m. = standard deviation/√N calculated using all individual ratios measured throughout the analysis region (Appendix A7).
(b) Small error likely fortuitous. Average expt. ID measurement error of ~ ±18‰ adopted for Fig. 2.

Table 3 References: [1] Swindle et al., 1986 [2] Becker & Pepin, 1984 [3] Meshik et al., 2014

Table 4: ID#25269 Xenon Corrected for Spallation and $(n,\gamma\beta^-)$ Products

	124/132	126/132	128/132	129/132	130/132	131/132	134/132	136/132
Measured (Table 3)	0.00464	0.00418	0.07459	2.5221	0.15369	0.8125	0.4026	0.3451
Total error[(a)]	0.00028	0.00048	0.00080	0.0063	0.00098	0.0031	0.0027	0.0023
δ wrt solar Xe [‰]	-51	-5	-114	1423.9	-67.4	-15.9	88.6	149.3
error [‰]	58	115	10	6.5	6.2	4.0	7.5	7.8
Spallation composition[(b)]	0.609	≡1	1.509	1.765	0.662	3.19	0.031	0
error	0.007		0.023	0.043	0.014	0.15	0.001	
Measured minus spallation	0.00395	0.00310	0.07277	2.5221	0.15293	0.8090	0.4026	0.3451
Δ wrt measured Xe	-0.00069	-0.00108	-0.00183	0	-0.00076	-0.0035	0	0
Δ/measured Xe [‰]	-149	-258	-24.4	0	-4.9	-4.3	0	0
Measured minus $(n,\gamma\beta^-)$[(c)]	0.00464	0.00418	0.07451	2.5221	0.15369	0.7916	0.4026	0.3451
Δ wrt measured Xe	0	0	-0.00008	0	0	-0.0209	0	0
Δ range wrt measured Xe			~0 -.00081			-0.0163 -0.0753		
Δ/measured Xe [‰]	0	0	-1.1	0	0	-26	0	0
Δ range/measured Xe [‰]			0/-10.9			+20/-93		
Corrected ID#25269	0.00395	0.00310	0.07269	2.5221	0.15293	0.7882	0.4026	0.3451
± uncertainty	0.00028	0.00048	+.00080 -.00108	0.0063	0.00098	+0.0166 -0.0754	0.0027	0.0023
δ wrt solar Xe [‰]	-192	-262	-136.7	1424.0	-72.0	-45.3	88.6	149.3
± uncertainty [‰]	58	115	+9.8 -13.0	6.5	6.2	+20.2 -91.3	7.5	7.8
δ wrt fract. solar Xe [‰]	81	-81	-1.1	1704	-1.8	-9.9	12.0	-6.7
uncertainty [‰]	78	143	+11.8 -15.4	10	6.9	+20.9 -94.7	7.2	7.5
Fract. solar wrt solar [‰]	-253	-196	-135.7	-103.6	-70.3	-35.8	75.7	157.0
uncertainty [‰]	14	19	4.1	2.5	2.8	2.1	3.0	4.7

(a) See Table 2, footnote (b).
(b) Spallation $^{132}Xe/^{126}Xe = 0.504 \pm 0.013$. Degassed spallogenic contributions to atmospheric ^{132}Xe and ^{129}Xe inventories are negligible, 0.5‰ and 0.7‰ respectively. Neither of these is included in spallation corrections to measured $^{M}Xe/^{132}Xe$ ratios.
(c) For $^{127}I(n,\gamma\beta^-)^{128}Xe$, ^{127}I = 100ppb ± a factor 10. For $^{130}Ba(n,\gamma\beta^-)^{131}Xe$ and Ba = 602ppm, adopted ^{131}Xe production rate (PR) = log average of the Hohenberg et al. (1978) and Rao et al. (2002) PRs. Upper and lower Δ ranges calculated for each of these PRs separately.

Appendix A. Supplementary material

1. Mass discrimination calculations.

1.1 Xenon.

Measured abundance of each isotope was referenced to that of ^{132}Xe. Comparison of isotope ratio data obtained in a static QMS calibration investigation to the actual calibration gas ratios indicated instrumental transmission bias favoring lighter isotopes, as shown in Fig. A1.1a. The linearity of this relationship leads to a simple function to correct for mass discrimination:

$$^{m}F = am + b \qquad (1)$$

where ^{m}F is the correction factor for the ratio of Xe isotope of mass m relative to ^{132}Xe (i.e.,$^{m}Xe/^{132}Xe$). To obtain a value and error of intercept b appropriate for Xe discrimination corrections, mass m = 124 was repositioned to m = 0 for intercept calculation. Corresponding coefficients of the linear fit are then a = -0.0087 ± 0.0010 and b = 1.0577 ± 0.0073. However this fit to the QMS data returns a value for $^{132}F < 1$, so relative to the base ^{132}Xe isotope, discriminations are given by $^{m}F/^{132}F$, with m = 0 for 124, 2 for 126, 4 for 128, and similarly for the remaining isotopes in Eq. (1). The correction factor was then applied using

$$^{m}R_c = {}^{m}R/(^{m}F/^{132}F) \qquad (2)$$

where ^{m}R is the isotope ratio as measured (incorporating corrections for dead time, background, and peak shapes) and $^{m}R_c$ is the isotope ratio corrected for mass discrimination, including errors introduced by uncertainties in a and b.

1.2 Krypton.

The same method, with m = 80 repositioned to 0 for intercept calculation, was used to derive analogous mass discrimination corrections for Kr isotope ratios referenced to ^{84}Kr (Fig. A1.1b).

Corrections have the form of Eq. (1), with coefficients a = -0.0173 ± 0.0024 and b = 1.0640 ± 0.0085. They were applied, with m = 0 for 80, 2 for 82, and so on for the remaining isotopes in Eq. (1), to the measured $^{m}Kr/^{84}Kr$ ratios by $^{m}R_c = ^{m}R/(^{m}F/^{84}F)$, the Kr equivalent of Eq. (2), including errors introduced by uncertainties in a and b.

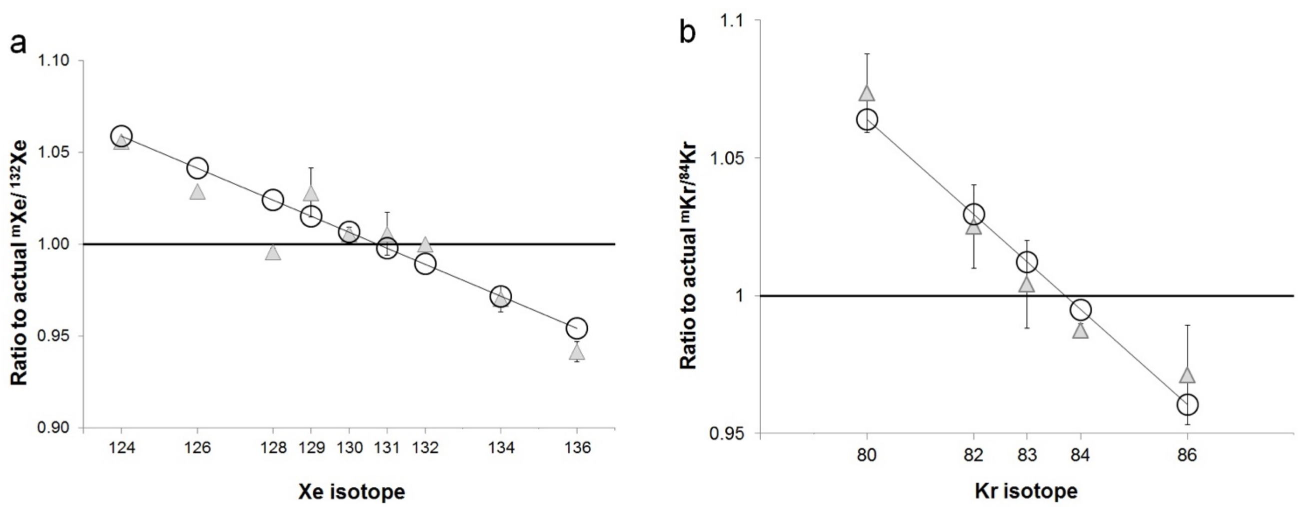

Figure A1.1. Derivation of mass discrimination correction functions from QMS calibration data for (a) Xe and (b) Kr. Triangles show ratios and errors of measured $^{m}Xe/^{132}Xe$ and $^{m}Kr/^{84}Kr$ relative to corresponding isotope ratios in the calibration gas represented by horizontal lines at y = 1. Least-square linear fits to the triangular data points return the values and uncertainties of slopes and intercepts used to calculate discrimination factors (Secs. A1.1, A1.2), shown here by circles. Calibration data for Xe (a) are more precise than those for Kr (b). Xe measurement errors are plotted where they exceed the triangular symbol sizes. Larger errors reflect effects of non-statistical stochastic interferences by instrumental background contaminants, particularly at ^{129}Xe and ^{131}Xe. Measured value for ^{128}Xe is clearly anomalous and was not included in the least-squares fit to the data.

1.3 Mass spectra

The mass spectra of both krypton and xenon as taken from the SAM experiment ID#25269 are shown in fig. A1.2. The Kr isotopes were obtained with semi-static mass spectrometry and are shown in panel A. The Xe spectrum, panel B, was acquired with the static mass spectrometry portion of the experiment as explained in Sec. 2.1.

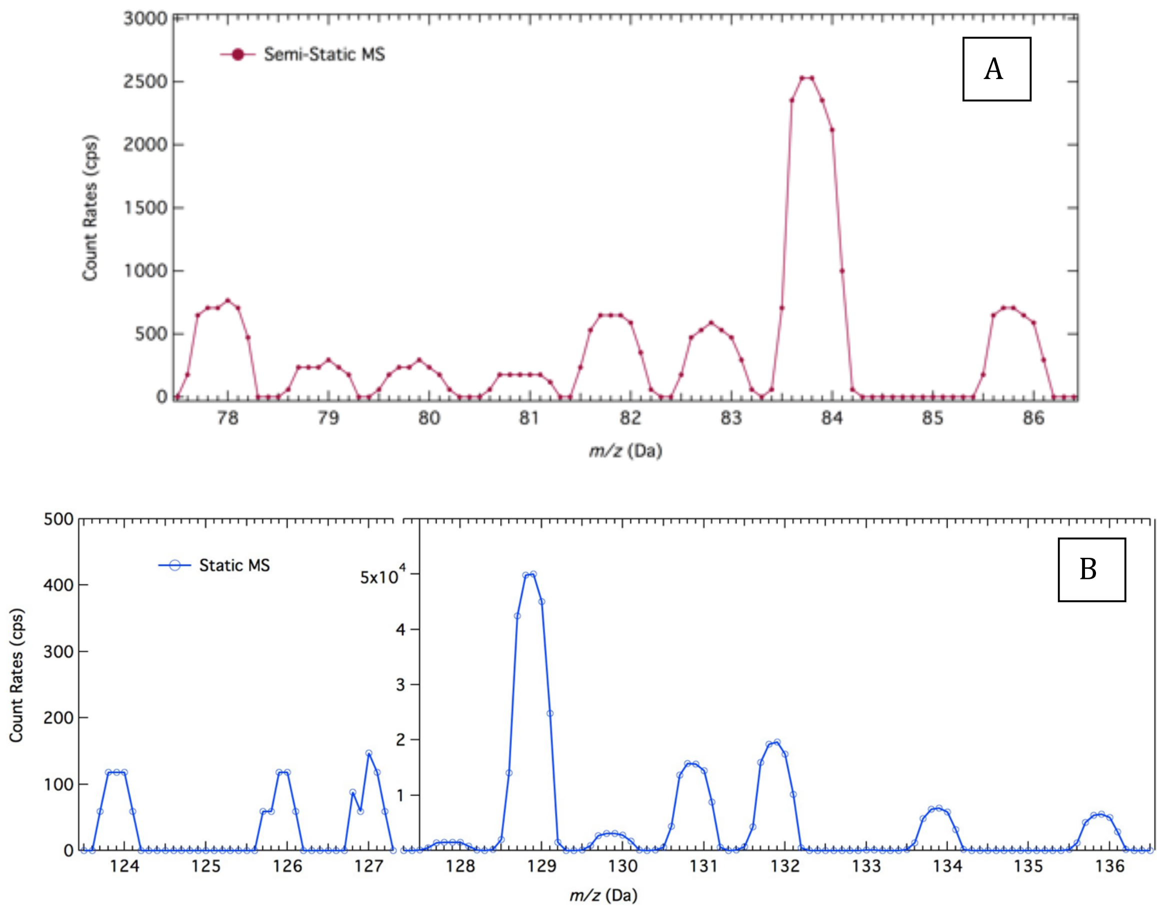

Figure A1.2. The mass spectra of (A) krypton and (B) xenon from experiment ID#25269. Kr spectrum acquired in semi-static mode and Xe in static mode. Neither are background corrected.

2. Xe hydride interferences:

Low-abundance ^{130}Xe, one mass unit above the large radiogenic ^{129}Xe abundance, is uniquely positioned in the Xe mass spectrum for potential interference from the ^{129}XeH hydride. Hydrogen abundances in background assays before and after the static Xe analyses are high.

Repeated measurements of background-corrected ^{133}Xe/^{132}Xe during the ID#25269 Xe analysis yield an average of 0.00175 ± 0.00028. This value provides a measure of the ^{132}XeH/^{132}Xe hydride, and therefore of the general hydride ratio ^{M}XeH/^{M}Xe. Application of this ratio to the ^{129}Xe-^{130}Xe pair in the 1/σ^2-weighted average of expt IDs #25253 and #25269, and to the more precisely measured ID #25269 alone, resulted in ~30‰ downward corrections of measured δ^{130}Xe upon removal of the interferences, to within < 4‰ of the SW fractionation curve (Table 2. Fig. 1). Hydride contributions to all other Xe isotopic abundances are either absent or negligible.

3. Possible hydrocarbon interferences:

3.1 Xenon

It is difficult to argue that MTBSTFA (Sec 3.1) is the source of the significant departure of m124 and m126 from the trend of fractionated solar wind. There are no fragments from MTBSTFA composition at m124. One might argue that MTBSTFA decomposition fragments could affect all of the other Xe isotopes, however we have calculated those effects, and even in the case of m126, they are very small. We determined a total background for each mass based on the values calculated for the background at the start of the static portion (before the Xe was admitted to the QMS) plus contributions due to MTBSTFA decomposition fragment products as measured by contributions of those fragments above their own background values in the static region. One such fragment is present at m127, used for trending background corrections, and others are present at m133, m135 & m147. The effects of the background subtraction of the MTBSTFA fragment masses are:

- At m124 – no effect because there is no MTBSTFA product at that mass.

♦ For other isotopes – generally the same as the trending background based on m127only.

We conclude that MTBSTFA is not a supportable explanation for the enrichment of ^{124}Xe and ^{126}Xe.

3.2 Krypton

One could argue that the large (754 ± 137 ‰) excess of the trace isotope ^{80}Kr relative to SW-Kr could reflect a mass interference from either hydrocarbons and/or sulfur species at mass 80. However, ^{82}Kr, for which there is no plausible interfering species, is also significantly enriched (Fig. 2).

4. Isotope ratio data over time

Example plots of individual Kr and Xe ratio measurements vs. time are shown for each of the experiments. These were selected to visually display data scatter for both low and high abundance isotope measurements (^{124}Xe/^{132}Xe, ^{131}Xe/^{132}Xe and ^{129}Xe/^{132}Xe, ^{80}Kr/^{84}Kr and ^{86}Kr/^{84}Kr). Each is labeled by the ratio vs. time display segment used to calculate the mean ratio and its statistical uncertainties. For the Kr data from experiment ID # 25111, “scrub” refers to each successive CO_2 and H_2O scrubber pass.

Xenon

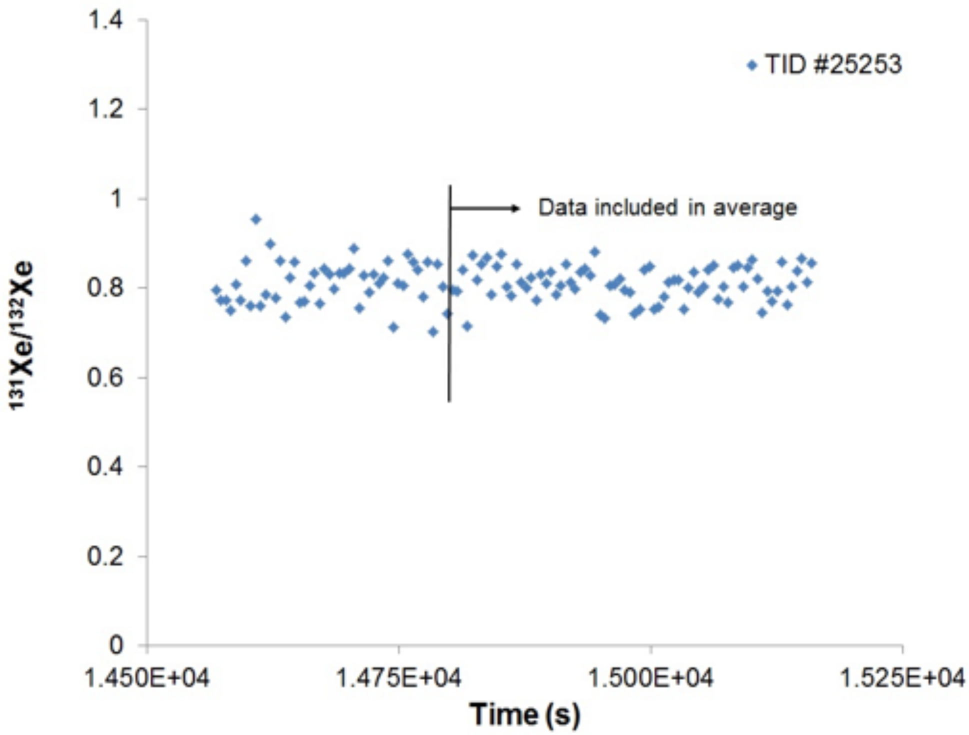
TID #25253
Data included in average
$^{131}Xe/^{132}Xe$
1.4
1.2
1
0.8
0.6
0.4
0.2
0
1.450E+04
1.475E+04
1.500E+04
1.525E+04
Time (s)

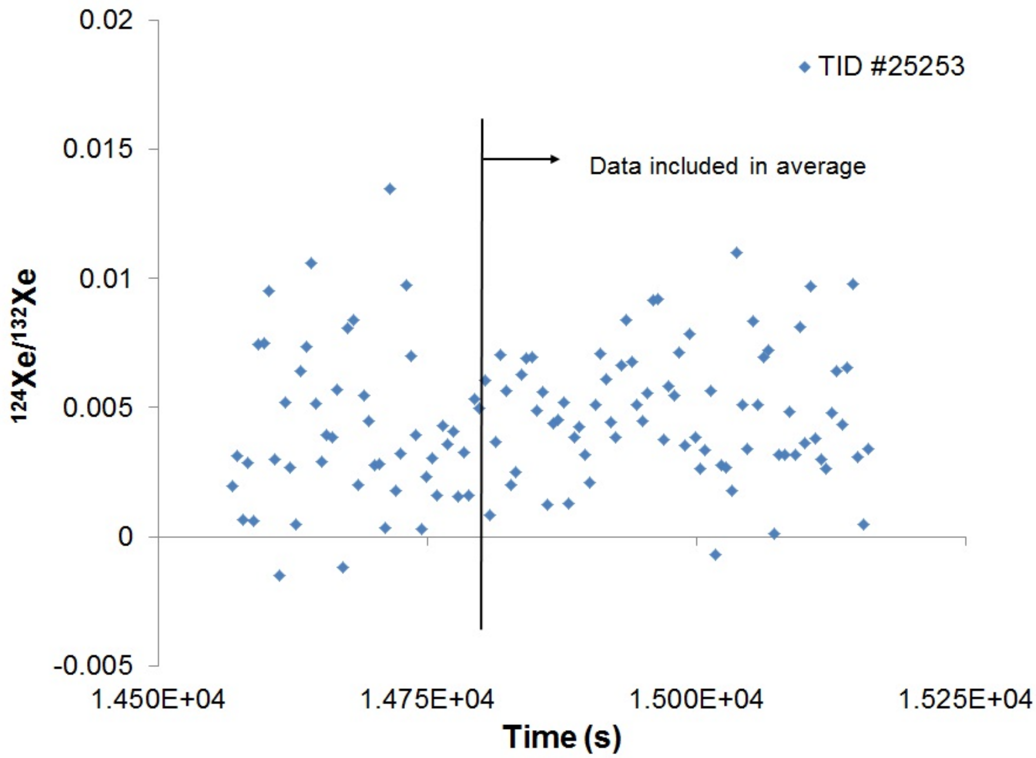
TID #25253
Data included in average
$^{124}Xe/^{132}Xe$
0.02
0.015
0.01
0.005
0
-0.005
1.450E+04
1.475E+04
1.500E+04
1.525E+04
Time (s)

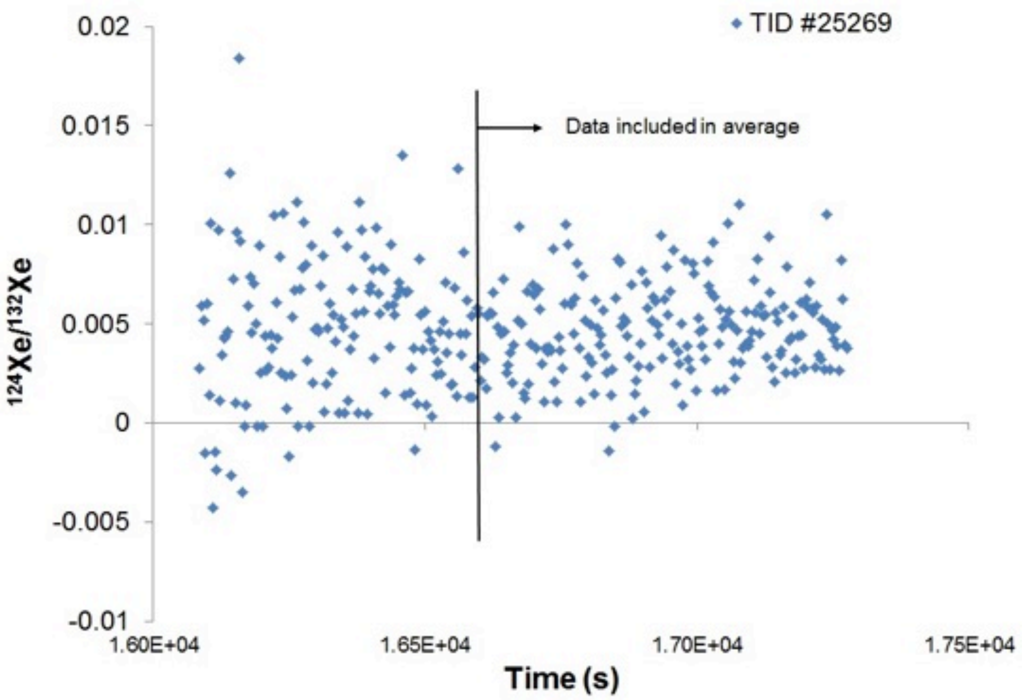
TID #25269
Data included in average
$^{124}Xe/^{132}Xe$
0.02
0.015
0.01
0.005
0
-0.005
-0.01
1.60E+04
1.65E+04
1.70E+04
1.75E+04
Time (s)

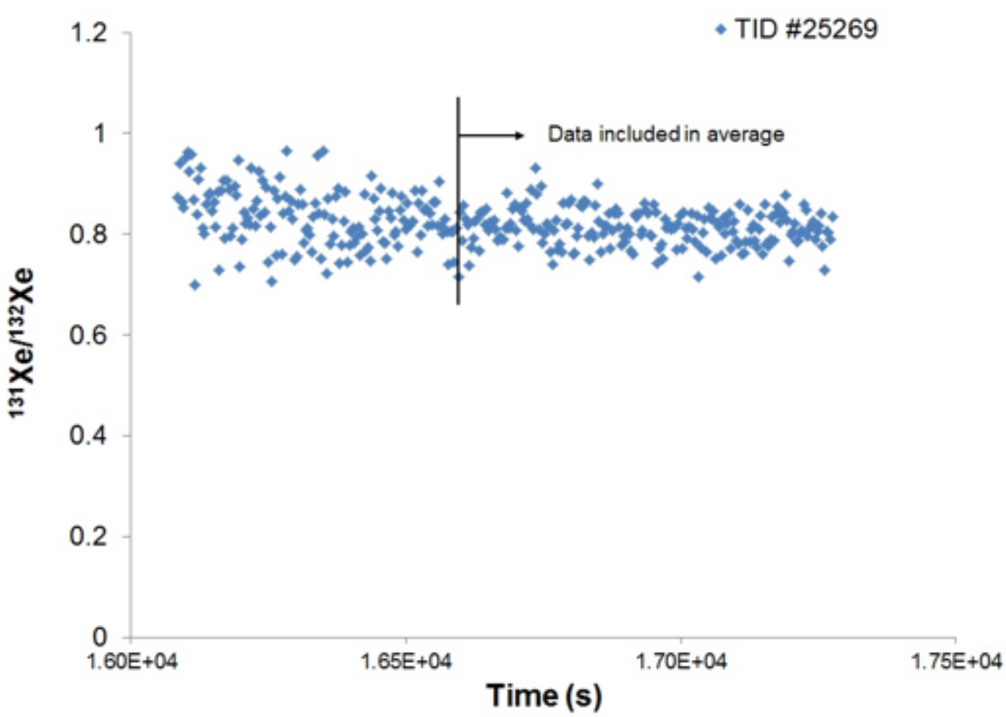
TID #25269
Data included in average
$^{131}Xe/^{132}Xe$
1.2
1
0.8
0.6
0.4
0.2
0
1.60E+04
1.65E+04
1.70E+04
1.75E+04
Time (s)

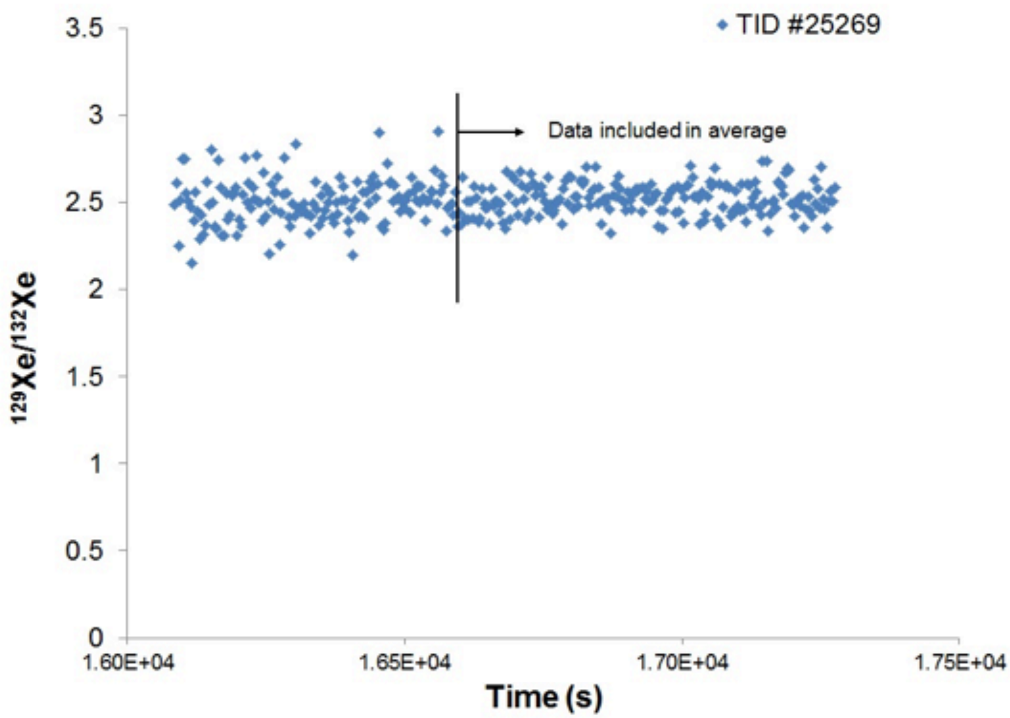
TID #25269
Data included in average
$^{129}Xe/^{132}Xe$
3.5
3
2.5
2
1.5
1
0.5
0
1.60E+04
1.65E+04
1.70E+04
1.75E+04
Time (s)

Krypton

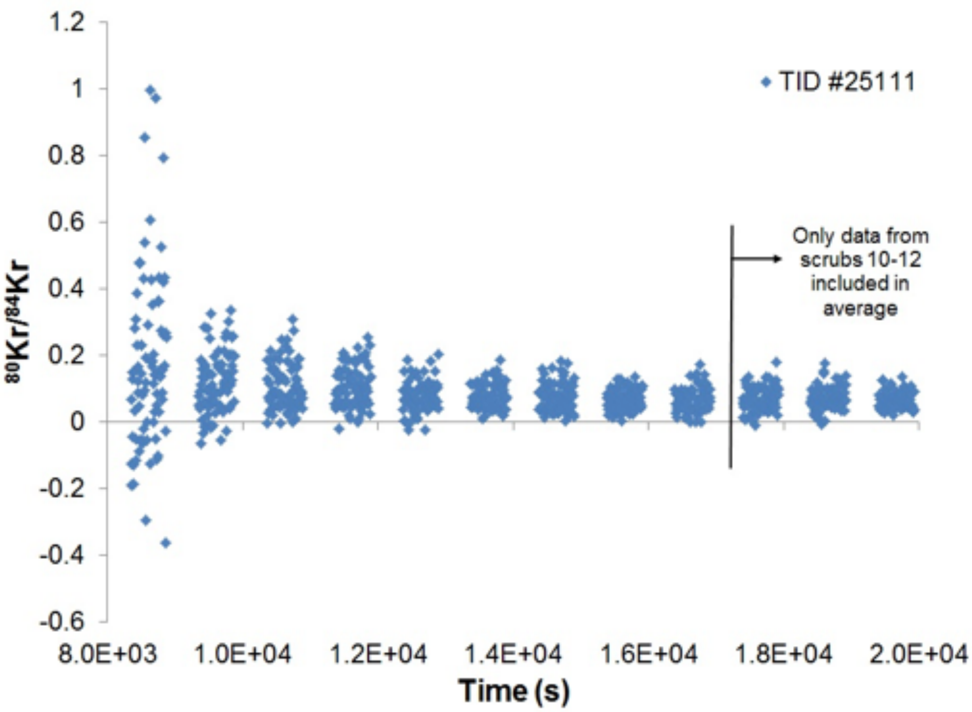
TID #25111
Only data from scrubs 10-12 included in average
$^{80}Kr/^{84}Kr$
1.2
1
0.8
0.6
0.4
0.2
0
-0.2
-0.4
-0.6
8.0E+03
1.0E+04
1.2E+04
1.4E+04
1.6E+04
1.8E+04
2.0E+04
Time (s)

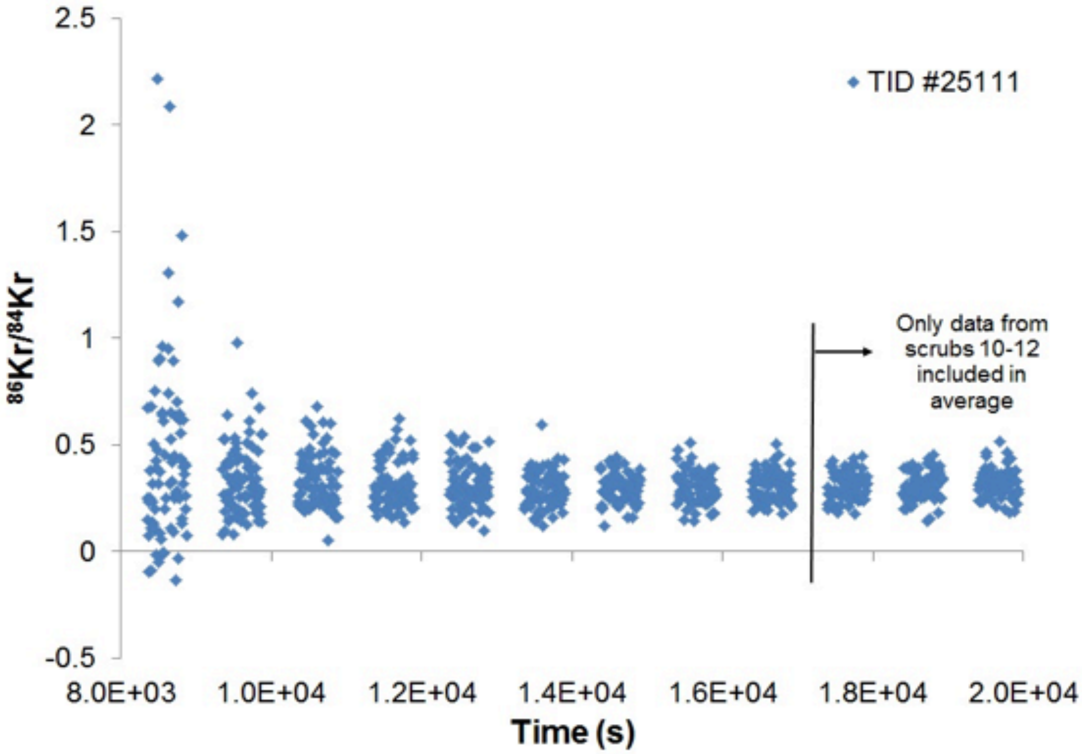
TID #25111
Only data from scrubs 10-12 included in average
$^{86}Kr/^{84}Kr$
Time (s)
2.5
2
1.5
1
0.5
0
-0.5
8.0E+03
1.0E+04
1.2E+04
1.4E+04
1.6E+04
1.8E+04
2.0E+04

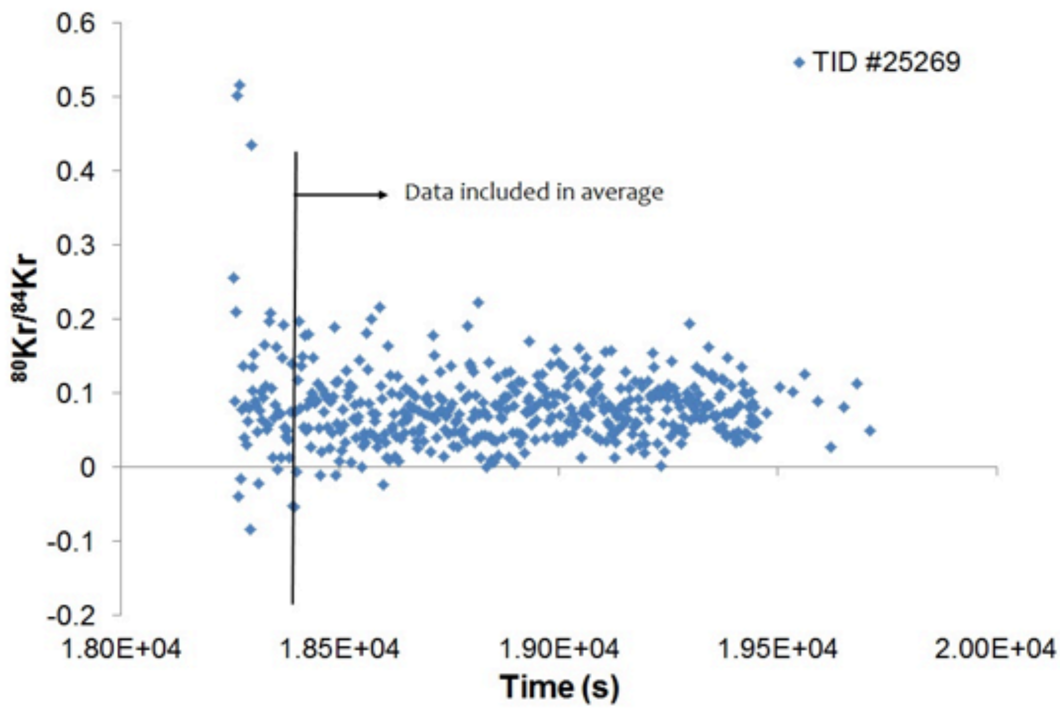
TID #25269
Data included in average
$^{80}Kr/^{84}Kr$
Time (s)
0.6
0.5
0.4
0.3
0.2
0.1
0
-0.1
-0.2
1.80E+04
1.85E+04
1.90E+04
1.95E+04
2.00E+04

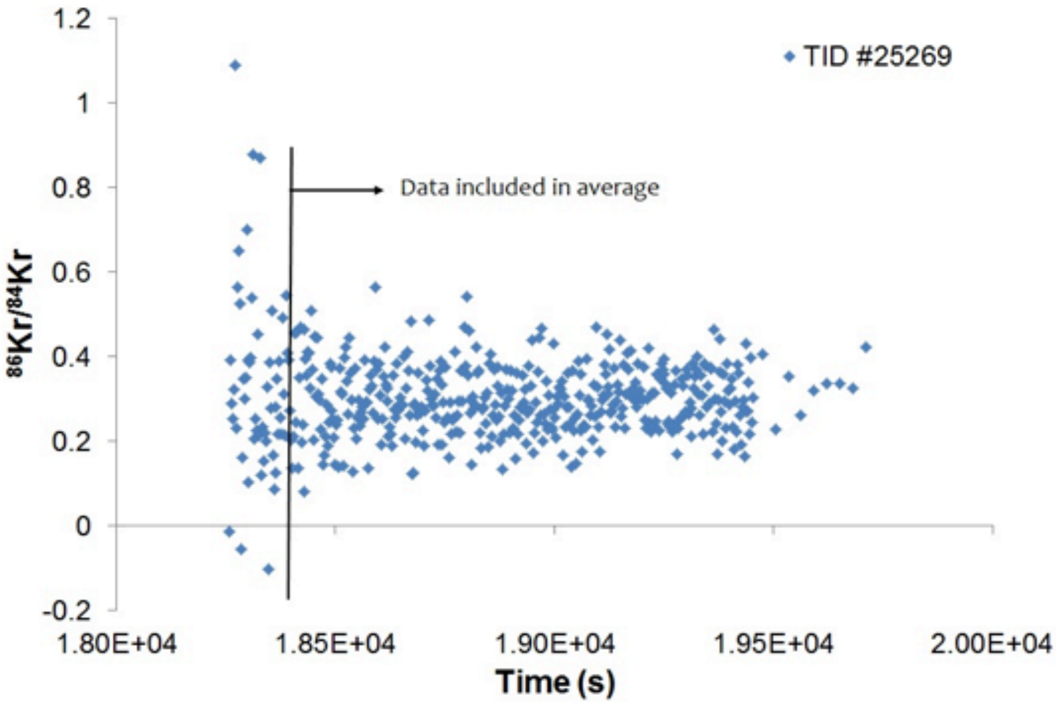

The SAM instrument measures backgrounds before ingesting the atmospheric samples and again after the QMS is evacuated, so we know that there are no memory effects that would affect the isotope ratios of subsequent experiments. Each experiment has telemetry markers that allow us to recognize valve positions, pressure and other instrument health data over time.

5. Atmospheric fission Xe on Mars?

Attempts to reveal a possible presence of atmospheric fission Xe assume a smaller degree of SW fractionation than that shown in Figs. 1 and 3. The resulting offsets of measured heavy isotope ratios from the revised fractionation curve can accommodate a component roughly resembling ^{244}Pu-Xe (Swindle and Jones, 1997; Mathew et al., 1998). Combined SAM and meteorite ratio data can be used to constrain this model of extant but fortuitously invisible fission Xe with relatively high precision. Unweighted averages of spallation-corrected ID#25269 data and the EETA79001 (Swindle et al., 1986) and EETA79001+Zagami (Mathew et al., 1998) Xe compositions (Tables 2 and 4), all renormalized to ^{130}Xe which has no fission Xe contribution, have ±1σ standard deviations of ≤ 9‰ for the $^{128,131\text{-}136}$Xe/^{130}Xe isotope ratios. Fig. A5.1 displays the fit of these averaged measured ratios to the SW fractionation curve A, taken from Fig. 1, which closely matches the meteorite and corrected SAM atmospheric data (Sec. 3.1, Fig. 4). Fig. A5.1 also shows a smaller fractionation B of solar Xe which, if applicable to Mars, would represent the composition of the atmosphere at the conclusion of the fractionating loss episode. The hypothesis that a fission Xe component is extant in the present atmosphere posits that the gaps between these two compositions at $^{131\text{-}136}$Xe were filled by degassing of ^{244}Pu-Xe after atmospheric Xe loss had terminated.

There are two constraints on such models: [1] the derived fission Xe composition must match Pu-Xe, and [2] measured light isotope ratios $^{124\text{-}128}$Xe/^{130}Xe cannot be perturbed beyond their error limits by the modeling assumptions. The latter constraint reflects the absence of fission contributions to the shielded isotopes ^{124}Xe, ^{126}Xe, ^{128}Xe and ^{130}Xe, so a successful model of fission Xe addition does not generate significant offsets from measured ratios at these isotopes.

Fig. A5.2 illustrates the ‰ differences between the averaged measured ratios and fractionation A. The close correspondence of measured ratios with A is evident. Nominal deviations are ≤ 8‰ for ^{131}Xe and ≤4‰ for all other isotopes (except radiogenic ^{129}Xe) heavier than ^{126}Xe, within ±1σ errors of zero except for ~1.7σ departures at ^{126}Xe and ^{131}Xe. This agreement suggests that fractionation A of fission-free solar Xe by itself accurately represents the composition of Mars' atmosphere. There is no apparent evidence for a fission Xe component in the system. It would be allowed only if addition of Pu-Xe to less fractionated solar Xe (e.g., fractionation B in Fig. 5A.1) yields $^{131\text{-}136}$Xe/^{130}Xe ratios consistent with their measured values.

There are two ways to assess whether a smaller solar Xe fractionation can accommodate the presence of a fission Xe component with Pu-Xe composition. One could first take the fractionation A fit to the data as accurate measures of atmospheric heavy isotope ratios. In this case the offsets plotted in Fig. A5.2 between fractionation A in Fig. A5.1 and the less fractionated solar Xe shown by the dotted curve B —chosen to marginally satisfy constraint [2] as discussed below— are not in accord with added Pu-Xe at the heavy isotopes. When translated to ^{M}Xe/^{136}Xe ratios these offsets yield ^{131}Xe/^{136}Xe = 0.385, ^{132}Xe/^{136}Xe = 0.965, and ^{134}Xe/^{136}Xe = 0.765 for the fission composition, values that diverge substantially, particularly at ^{134}Xe/^{136}Xe, from ^{244}Pu fission yields of 0.248 ± 0.015, 0.893 ± 0.013, and 0.930 ± 0.005 respectively (Hudson et al., 1989). Differences are not reduced by adjusting the fractionation A fit to the extent allowed by errors in measured ratios (Fig. A5.2) nor by assuming smaller degrees of solar Xe fractionation in B which increase its divergences from A. It appears that Xe ratios in the added component calculated in this way fail to satisfy constraint [1]; they are incompatible with ^{244}Pu fission, and also with spontaneous and neutron-induced fission of ^{238,235}U.

Constraint [2] on light isotope perturbations effectively controls the model. With present data the scatter and errors of the $^{124\text{-}126}$Xe/^{130}Xe measurements are too large to be useful. However average measured δ^{128}Xe/^{130}Xe with respect to SW-Xe falls squarely on the fractionation A curve (Fig. A5.2) and is sufficiently precise —±1σ standard deviation of 4.6‰, including error contributed by normalization to SW-Xe— to severely restrict the possible range of fractionation B relative to A. The dotted curve in Figs. A5.1,2 was selected to pass through the +1σ uncertainty in measured $^{128}Xe/^{130}Xe$ (Fig. A5.2). In this limiting case one can explore in a different way the effects of a fission component added to B. The discussion above demonstrates that A minus B calculations yield results incompatible with ^{244}Pu-Xe. However, by hypothesis, the residual Xe composition in the atmosphere following the loss episode is now *not* represented by fractionation A, but by B instead. This suggests an alternate approach in which the fission Xe composition is *assumed* to satisfy constraint [1], i.e., to be ^{244}Pu-Xe, and effects of its addition to B are compared, not to A, but to the actual measured heavy-isotope ratios.

Results are shown by the filled black circles in Fig. A5.2. Addition to B of sufficient Pu-Xe to replicate the measured $^{136}Xe/^{130}Xe$ ratio also generates $^{131-134}Xe/^{130}Xe$ ratios that fall close to or within the 1σ error bars of measured values, and very close to A. In other words the combination of fractionation B plus Pu-Xe precisely mimics the measured isotopic distributions —except for $^{128}Xe/^{130}Xe$— that underlie the fractionation A fit to the data. In this limit of measured $^{128}Xe/^{130}Xe$ there could indeed be a hidden Pu fission component in Mars' atmosphere.

However the amount of this fission Xe is very small. Comparisons with extinct radionuclide products in Earth's atmosphere are informative. There the abundance of ^{136}Xe from ^{244}Pu, in units of mol/g-Earth, is 1.1 x 10^{-17} (Pepin, 1991, 2000). The hidden fission ^{136}Xe abundance derived above for Mars' atmosphere is only 6.2 x 10^{-20} mol/g-Mars, so to the extent that initial g-Pu/g-planet inventories and closure times for gas loss to space were similar for Earth and Mars, only 0.6% of the available Pu-^{136}Xe on Mars is in the atmosphere. Initial U-Pu concentrations in models of Mars' bulk composition differ from Earth values by less than a factor 2 (Lodders and Fegley, 1997), so 0.6% should be valid to within this factor. If the adopted ±1σ error limit in measured $^{128}Xe/^{130}Xe$ were expanded to ±2σ, the corresponding fractionation B curve through +2σ in Fig. A5.2 would yield twice the 0.6% ratio, larger but still minor. Effects of differences in gas-loss closure times between the two planets can be estimated from the Pu-Xe closure age equation (Pepin and Porcelli, 2006) modified to allow variable degassing fractions from the martain silicate mantle, and Pepin and Porcelli's calculated Earth closure at ~96Ma. When assumed closure times for Mars are varied from twice to ≤ half of Earth's closure age, the corresponding fractions of total mantle Pu-^{136}Xe inventories currently residing in the atmosphere range from ~0.7% to ≤ ~0.2%. These observations suggest that the two planets experienced radically different outgassing histories, on Mars facilitating early release of ^{129}Xe from decay of short-lived ^{129}I but efficiently throttling later degassing of interior Xe from fission of ~5x longer-lived ^{244}Pu, a possibility previously noted by Mathew et al. (1998).

The atmospheric fission Xe contributions derived from this modeling are upper limits since by constraint [2] their existence depends on assuming a $^{128}Xe/^{130}Xe$ ratio at the 1σ or 2σ upper bounds of its measured value. They would be restricted still further if the 2.3‰ s.e.m. of the three $^{128}Xe/^{130}Xe$ measurements were adopted instead of the larger standard deviation of an individual measurement. One could argue, from the fact that the nominal $^{128}Xe/^{130}Xe$ ratio in Fig. A5.2 differs from the fractionation A curve by only 0.2‰, that an atmospheric fission component is most likely either absent or undetectably negligible. However it hardly matters whether this or an upper-limit view is taken. By whatever measure, Pu-Xe appears to be, at most, a minor constituent of the atmosphere, and the near absence of the abundance expected for correlated degassing of ^{129}I and

^{244}Pu decay products remains to be fully explained. And, even in the scenario evaluated above, >98% to 100% of nonradiogenic atmospheric Xe still derives from a mass fractionation of solar Xe close to fractionation A.

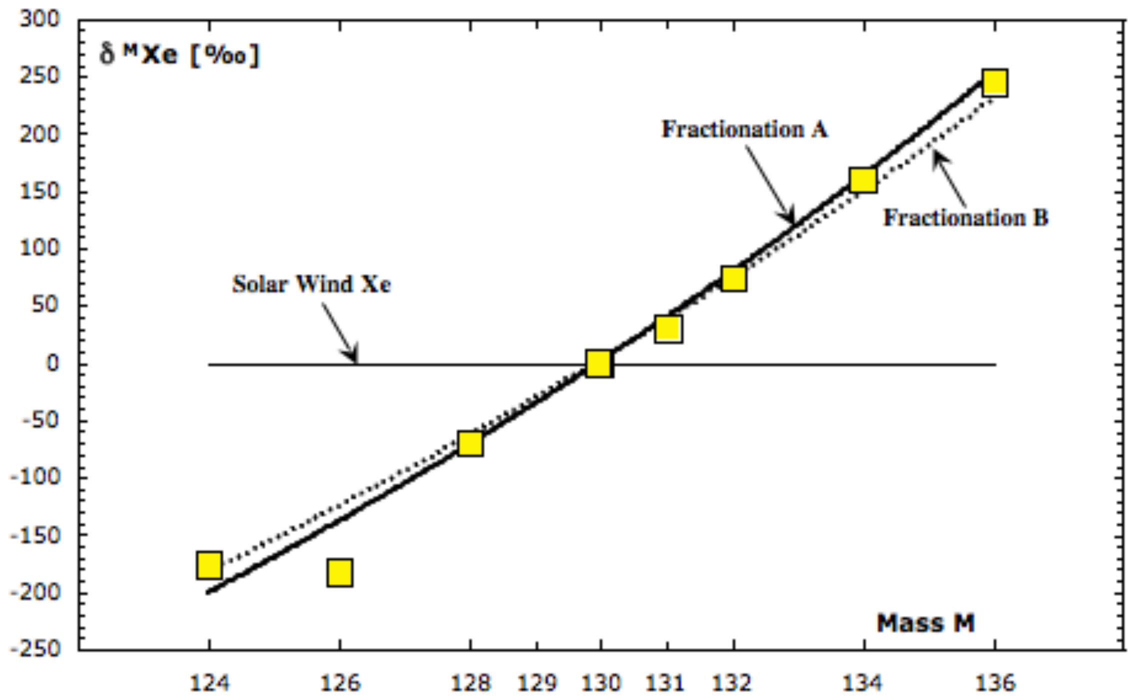

Fig. A5.1. Unweighted averages (yellow squares) of spallation-corrected ratios in ID#25269 (Table 4) and the shergottite glasses (Table 2), plotted as δ-values with respect to SW-Xe. All ratio data normalized to ^{130}Xe. Fractionation A is the re-normalized SW fractionation curve shown in Fig. 1, generated for $f_{124/130} = 0.8035$ (see Appendix 6). The dotted fractionation B curve ($f_{124/130} = 0.8150$) represents a less severe fractionating loss of solar Xe. The $^{M}Xe/^{130}Xe$ ratios in the atmosphere that would pertain at the end of this atmospheric escape episode fall along the dotted curve.

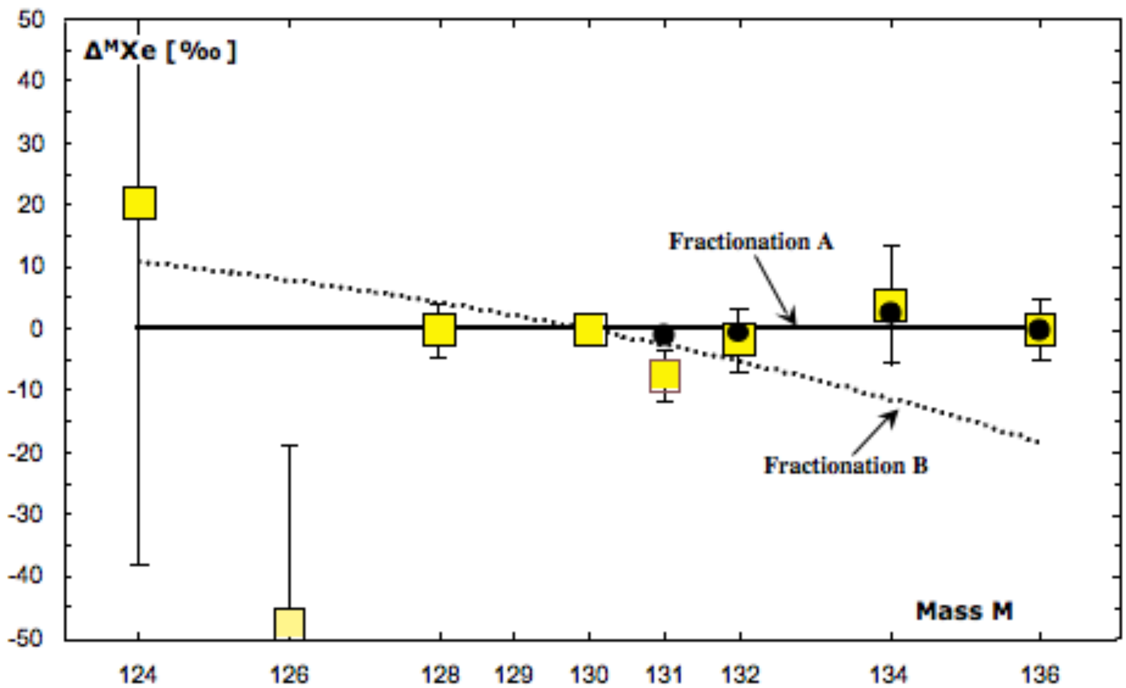

Fig. A5.2. Differences Δ^MXe in ‰ between average measured δ-^{M}Xe/^{130}Xe ratios and fractionation A in Fig. A5.1 (yellow squares with $\pm 1\sigma$ error bars), and between the composition predicted by fractionation B relative to A for B constrained to pass through measured ^{128}Xe/^{130}Xe plus 1σ (dotted curve). Filled black circles show compositions obtained by adding ^{244}Pu-derived fission Xe to fractionation B.

Added references for Appendix A5

Hudson, G. B., Kennedy, B. M., Podosek, F. A., Hohenberg, C. M. 1989. The early solar system abundance of ^{244}Pu as inferred from the St. Severin chondrite. Proc. 19th Lunar Planet. Sci. Conf., 547-557.

Lodders, K., Fegley, B. Jr. 1997. An oxygen isotope model for the composition of Mars. Icarus 126, 373-394.

Pepin, R. O., Porcelli, D. 2006. Xenon isotope systematics, giant impacts, and mantle degassing on the early Earth. Earth Planet. Sci. Lett. 250, 470-485.

6. Isotopic fractionation factors for fractionated solar wind

These are derived from the expression describing depletions in atmospheric inventories during hydrodynamic escape under conditions of constant hydrogen inventory (Eq. (12) in Pepin 1991). Eq. 12 yields solutions for the escape depletion factors $f_M = N_M/(N_M)_0$, where N_M is the atmospheric inventory of species M and its initial value is indicated by subscript 0. For Xe isotopes M, dividing Eq. 12 by the depletion factor for escaping $^{130}Xe = f_{130} = N_{130}/(N_{130})_0$ gives $[N_M/(N_M)_0]/[N_{130}/(N_{130})_0] = (N_M/N_{130})/(N_M/N_{130})_0 = f_{M/130}$, the Xe isotopic fractionation factors. Calculated $f_{M/130}$ factors are logarithmic in M (denoted in Eq. 12 by m_2) where $f_{136/130} = 1/f_{124/130}$. They are independent of values for all other input variables in Eq. 12 and are also insensitive to the choice of hydrodynamic loss model, either at constant inventory as described by Eq. 12 or by Rayleigh distillation (Eq. (16) in Pepin 1991). The latter can replicate $f_{M/130}$ values derived from the constant inventory model to within ≤ 2‰.

Their logarithmic dependence allows fractionation factors $f_{M/130}$ for any chosen value of $f_{124/130}$ to be readily calculated from a 2-point logarithmic fit to $(124, f_{124/130})$ and $(136, 1/f_{124/130})$, which returns an equation of the form $f_{M/130} = Ae^{B*M}$ where values of both A and B depend on the selected $f_{124/130}$. An example curve of $f_{M/130}$ vs. M for an extreme fractionation of $f_{124/130} = 0.100$ is illustrated below. Symmetry dictates the choice of M = ^{130}Xe normalization, but $f_{M/130}$ fractionation factors are easily converted to $f_{M/132}$ by dividing $f_{M/130}$ by $f_{132/130}$. The SW fractionation curve in Figs. 1 and 3 was generated for $f_{124/130} = 0.8035$ (with an estimate variance in fit to the data of ± 0.0040), corresponding to $f_{124/132} = 0.7470 \pm 0.0050$. All $f_{M/132}$ values and their uncertainties are listed in Table 2. For fractionation B in Figs. A5.1,2 (Appendix A5), $f_{124/130}$ is 0.8150.

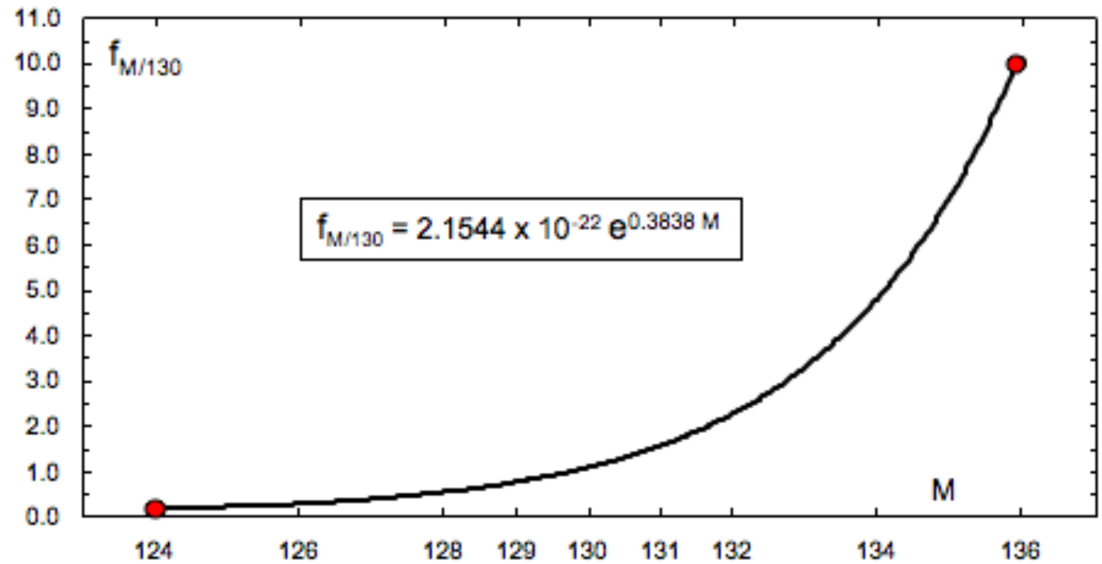

Fig. A6. Fractionation factors $f_{M/130}$ vs. isotope mass M for the extreme fractionation resulting from selection of $f_{124/130} = 0.1$ and $f_{136/130} = 1/\, f_{124/130} = 10$. Returned equation for $f_{M/130}$ displayed in the figure box.

7. Data files

In the table that follows all of the data are shown corrected for mass discrimination, peak shape and deadtime. The ratios for Xe are to ^{132}Xe and for Kr to ^{84}Kr, and all ratio data are rounded to four decimal places.

Experiment ID#25269 Xenon Isotopic Ratio Data

Time	$^{124}Xe/^{132}Xe$	$^{126}Xe/^{132}Xe$	$^{128}Xe/^{132}Xe$	$^{129}Xe/^{132}Xe$	$^{130}Xe/^{132}Xe$	$^{131}Xe/^{132}Xe$	$^{134}Xe/^{132}Xe$	$^{136}Xe/^{132}Xe$
16601.84	0.0021	0.0057	0.0749	2.3733	0.1430	0.7876	0.3590	0.3028
16605.26	0.0033	0.0017	0.0778	2.6405	0.1777	0.8570	0.4150	0.3511
16608.68	0.0032	0.0113	0.0804	2.4048	0.1474	0.8301	0.4547	0.3162
16612.10	0.0017	0.0026	0.0816	2.5041	0.1619	0.8176	0.4050	0.3269
16615.52	0.0054	0.0076	0.0820	2.4020	0.1391	0.7368	0.3840	0.3718
16618.94	0.0056	0.0007	0.0669	2.5047	0.1404	0.7747	0.4407	0.3408
16622.36	0.0055	0.0087	0.0771	2.4088	0.1517	0.7908	0.4008	0.3442
16625.78	0.0066	0.0064	0.0737	2.5905	0.1625	0.8254	0.3680	0.3612
16629.20	-0.0012	0.0096	0.0916	2.5246	0.1773	0.8309	0.4351	0.3787
16632.62	0.0048	0.0034	0.0768	2.3885	0.1515	0.7670	0.3514	0.3415
16636.04	0.0003	0.0011	0.0826	2.4063	0.1294	0.8443	0.3551	0.3487
16639.46	0.0045	0.0077	0.0859	2.5798	0.1434	0.8432	0.4001	0.3650
16642.88	0.0073	0.0030	0.0703	2.4900	0.1550	0.8185	0.4028	0.3562
16646.30	0.0046	0.0083	0.0625	2.4670	0.1586	0.8510	0.3798	0.3952
16649.72	0.0025	0.0006	0.0693	2.4750	0.1452	0.8069	0.4108	0.2861
16653.14	0.0029	0.0011	0.0781	2.3717	0.1424	0.8227	0.3709	0.3065
16656.56	0.0035	0.0020	0.0782	2.5790	0.1728	0.8232	0.4103	0.3329
16659.98	0.0020	0.0020	0.0701	2.4798	0.1423	0.8282	0.3879	0.3138
16663.40	0.0040	0.0070	0.0649	2.5077	0.1607	0.8096	0.3822	0.3574
16666.82	0.0003	0.0047	0.0656	2.5063	0.1654	0.7866	0.4122	0.3230
16670.24	0.0052	0.0020	0.0675	2.4401	0.1626	0.7945	0.3994	0.3419
16673.66	0.0099	0.0054	0.0673	2.4920	0.1285	0.7922	0.3672	0.3076
16677.08	0.0050	0.0032	0.0683	2.3784	0.1702	0.7898	0.4021	0.3464
16680.50	0.0015	0.0044	0.0675	2.3508	0.1310	0.8121	0.3799	0.3293
16683.92	0.0012	0.0016	0.0666	2.6759	0.1752	0.8810	0.4326	0.3568
16687.34	0.0066	0.0006	0.0581	2.5376	0.1435	0.8125	0.3620	0.3551
16690.76	0.0020	0.0052	0.0708	2.4039	0.1469	0.8204	0.3983	0.3382
16694.18	0.0040	0.0025	0.0775	2.6532	0.1810	0.8492	0.4356	0.3071
16697.60	0.0070	0.0026	0.0879	2.6303	0.1652	0.8584	0.4208	0.3576
16701.02	0.0065	0.0055	0.0724	2.5002	0.1654	0.8069	0.3847	0.3397
16704.44	0.0038	0.0023	0.0740	2.4246	0.1519	0.7754	0.4272	0.3167
16707.86	0.0068	0.0034	0.0718	2.6785	0.1544	0.8535	0.4804	0.3854
16711.28	0.0058	0.0056	0.0690	2.5959	0.1601	0.8454	0.4360	0.4012
16714.70	0.0030	0.0028	0.0732	2.5200	0.1626	0.8272	0.4215	0.3577
16718.12	0.0011	0.0057	0.0656	2.3992	0.1642	0.8622	0.3722	0.3511
16721.54	0.0037	0.0049	0.0746	2.5770	0.1602	0.8292	0.3970	0.3648
16724.96	0.0036	0.0060	0.0759	2.4412	0.1420	0.8185	0.3850	0.3245
16728.38	0.0038	0.0037	0.0773	2.6655	0.1530	0.8883	0.4130	0.3677
16731.80	0.0036	0.0102	0.0702	2.6082	0.1340	0.8094	0.4189	0.3448
16735.22	0.0088	0.0019	0.0707	2.5379	0.1708	0.9304	0.4034	0.3674
16738.64	0.0021	0.0042	0.0654	2.5874	0.1611	0.8798	0.4412	0.3667
16742.06	0.0011	0.0065	0.0928	2.4160	0.1691	0.8091	0.3947	0.2933
16745.48	0.0043	0.0020	0.0774	2.5899	0.1708	0.8960	0.4477	0.3709
16748.90	0.0037	0.0040	0.0672	2.5438	0.1667	0.7829	0.4316	0.3614
16752.32	0.0028	0.0056	0.0758	2.5027	0.1717	0.8009	0.3839	0.3969

16755.74	0.0060	0.0095	0.0852	2.4628	0.1325	0.8211	0.3824	0.3367
16759.16	0.0100	0.0059	0.0952	2.6452	0.1702	0.8158	0.4126	0.3737
16762.58	0.0090	0.0051	0.0602	2.4889	0.1549	0.7639	0.3884	0.3286
16766.00	0.0060	0.0030	0.0700	2.4367	0.1533	0.7388	0.3973	0.3610
16769.42	0.0059	0.0030	0.0668	2.4537	0.1563	0.8076	0.3553	0.3379
16772.84	0.0045	0.0073	0.0805	2.5074	0.1566	0.8286	0.4462	0.3270
16776.26	0.0063	0.0082	0.0822	2.4962	0.1546	0.7697	0.3902	0.3370
16779.68	0.0081	0.0140	0.0625	2.5170	0.1670	0.7794	0.3944	0.3396
16783.10	0.0038	0.0013	0.0953	2.3736	0.1592	0.7643	0.3366	0.3146
16786.52	0.0010	0.0054	0.0608	2.5801	0.1737	0.8619	0.3888	0.3403
16789.94	0.0074	0.0064	0.0899	2.6231	0.1648	0.8181	0.4252	0.3353
16793.36	0.0052	0.0046	0.0827	2.4896	0.1713	0.8199	0.4017	0.3357
16796.78	0.0024	0.0053	0.0874	2.6475	0.1731	0.8612	0.4365	0.3409
16800.20	0.0033	0.0097	0.0707	2.6446	0.1872	0.8682	0.4401	0.3275
16803.62	0.0049	-0.0003	0.0756	2.4584	0.1440	0.7610	0.4009	0.3559
16807.04	0.0031	0.0070	0.0694	2.5296	0.1695	0.7612	0.4187	0.3390
16810.46	0.0015	0.0030	0.0704	2.5332	0.1628	0.7965	0.4493	0.3643
16813.88	0.0062	0.0021	0.0685	2.4790	0.1346	0.8125	0.4407	0.3162
16817.30	0.0048	0.0055	0.0802	2.6264	0.1838	0.8562	0.4037	0.2930
16820.72	0.0039	0.0066	0.0703	2.6072	0.1553	0.8535	0.3954	0.3408
16824.14	0.0045	0.0052	0.0958	2.6269	0.1698	0.8656	0.4319	0.3502
16827.56	0.0057	0.0076	0.0716	2.7016	0.1634	0.8639	0.4439	0.3592
16830.98	0.0034	0.0033	0.0742	2.5255	0.1667	0.7953	0.4179	0.3457
16834.40	0.0025	0.0024	0.0632	2.4808	0.1381	0.7478	0.3693	0.3506
16837.82	-0.0014	0.0068	0.0770	2.5676	0.1765	0.8036	0.3921	0.3540
16841.24	0.0014	0.0053	0.0807	2.5790	0.1466	0.7932	0.4178	0.3794
16844.66	0.0027	0.0022	0.0720	2.7031	0.1706	0.8573	0.4308	0.3658
16848.08	-0.0002	0.0046	0.0714	2.4927	0.1449	0.8988	0.4300	0.3293
16851.50	0.0063	0.0043	0.0606	2.5859	0.1537	0.8244	0.3998	0.3517
16854.92	0.0083	0.0062	0.0842	2.3734	0.1743	0.7646	0.3848	0.3421
16858.34	0.0081	0.0040	0.0518	2.5160	0.1338	0.8015	0.3751	0.3190
16861.76	0.0049	-0.0014	0.0805	2.5019	0.1687	0.8160	0.3721	0.3200
16865.18	0.0053	0.0032	0.0987	2.5266	0.1701	0.8171	0.4140	0.3235
16868.60	0.0051	0.0050	0.0771	2.4615	0.1525	0.8415	0.3934	0.3704
16872.02	0.0044	0.0005	0.0791	2.3202	0.1536	0.7712	0.3605	0.3273
16875.44	0.0033	0.0070	0.0737	2.5376	0.1296	0.8067	0.4066	0.3158
16878.86	0.0070	0.0021	0.0802	2.6064	0.1657	0.8405	0.3933	0.3270
16882.28	0.0002	0.0032	0.0666	2.5335	0.1392	0.8508	0.3856	0.3367
16885.70	0.0014	0.0017	0.0717	2.6473	0.1670	0.8409	0.4228	0.3526
16889.12	0.0021	0.0081	0.0766	2.5781	0.1704	0.8143	0.3671	0.3852
16892.54	0.0029	0.0012	0.0823	2.5112	0.1367	0.7791	0.3983	0.3551
16895.96	0.0040	0.0110	0.0787	2.5017	0.1763	0.7954	0.3985	0.3496
16899.38	0.0077	0.0068	0.0799	2.4533	0.1521	0.7852	0.3857	0.3356
16902.80	0.0006	0.0032	0.0760	2.5557	0.1845	0.8118	0.4279	0.3828
16906.22	0.0071	0.0020	0.0731	2.5118	0.1642	0.8008	0.3773	0.3198
16909.64	0.0058	0.0056	0.0645	2.4567	0.1580	0.7657	0.4211	0.3384
16913.06	0.0028	0.0046	0.0714	2.5548	0.1692	0.7592	0.3876	0.3618
16916.48	0.0052	0.0024	0.0595	2.5773	0.1539	0.8386	0.4223	0.3583
16919.90	0.0063	0.0047	0.0777	2.5676	0.1656	0.8336	0.4011	0.3661
16923.32	0.0062	0.0036	0.0745	2.5798	0.1576	0.8415	0.4273	0.3589
16926.74	0.0049	0.0023	0.0618	2.4449	0.1669	0.7987	0.3635	0.3149
16930.16	0.0044	0.0062	0.0686	2.5856	0.1451	0.8064	0.4166	0.3248
16933.58	0.0095	0.0093	0.0688	2.5175	0.1722	0.8624	0.4449	0.3824
16937.00	0.0032	0.0054	0.0728	2.5626	0.1624	0.8480	0.3959	0.3603

16940.42	0.0063	0.0035	0.0772	2.5064	0.1695	0.8403	0.4213	0.3339
16943.84	0.0079	0.0043	0.0772	2.6022	0.1466	0.7992	0.4221	0.3413
16947.26	0.0055	-0.0010	0.0978	2.5120	0.1472	0.7952	0.3968	0.3235
16950.68	0.0067	0.0088	0.0658	2.5466	0.1409	0.8601	0.4170	0.3568
16954.10	0.0040	0.0020	0.0857	2.5520	0.1442	0.8428	0.4396	0.3390
16957.52	0.0087	0.0050	0.0769	2.3629	0.1515	0.7412	0.3891	0.3151
16960.94	0.0020	0.0005	0.0690	2.4538	0.1726	0.7704	0.4140	0.3257
16964.36	0.0036	0.0045	0.0733	2.3451	0.1430	0.7808	0.3767	0.3217
16967.78	0.0030	0.0015	0.0756	2.4502	0.1391	0.7515	0.3872	0.3402
16971.20	0.0050	0.0034	0.0704	2.5120	0.1610	0.8295	0.4424	0.3690
16974.62	0.0009	0.0069	0.0678	2.5272	0.1418	0.8128	0.4115	0.3409
16978.04	0.0082	0.0034	0.0690	2.5514	0.1433	0.8188	0.3957	0.3407
16981.46	0.0039	0.0027	0.0682	2.5681	0.1520	0.8107	0.4266	0.3581
16984.88	0.0032	0.0016	0.0663	2.5783	0.1714	0.8147	0.3916	0.3321
16988.30	0.0027	0.0043	0.0777	2.4433	0.1551	0.8129	0.4216	0.3270
16991.72	0.0080	0.0060	0.0740	2.5902	0.1582	0.7695	0.4000	0.3289
16995.14	0.0076	0.0052	0.0839	2.4499	0.1711	0.8208	0.4236	0.3668
16998.56	0.0017	0.0030	0.0753	2.5709	0.1680	0.8355	0.4220	0.3154
17001.98	0.0053	0.0058	0.0725	2.3820	0.1490	0.7716	0.3643	0.3484
17005.40	0.0046	0.0041	0.0768	2.5243	0.1590	0.8443	0.4044	0.3945
17008.82	0.0039	0.0030	0.0699	2.5951	0.1619	0.8118	0.4386	0.3752
17012.24	0.0047	0.0061	0.0856	2.5957	0.1967	0.7906	0.4446	0.3624
17015.66	0.0032	0.0087	0.0729	2.7077	0.1693	0.8140	0.4358	0.3576
17019.08	0.0082	0.0035	0.0723	2.6439	0.1463	0.8413	0.4362	0.3562
17022.50	0.0069	0.0064	0.0739	2.5308	0.1611	0.8091	0.3837	0.3492
17025.92	0.0066	0.0019	0.0791	2.5292	0.1692	0.7845	0.3852	0.3463
17029.34	0.0091	0.0033	0.0798	2.5158	0.1776	0.8370	0.3911	0.3572
17032.76	0.0063	0.0031	0.0637	2.3775	0.1284	0.7155	0.3880	0.3120
17036.18	0.0016	0.0033	0.0736	2.5601	0.1551	0.7738	0.3969	0.3437
17039.60	0.0040	0.0028	0.0749	2.3970	0.1456	0.8025	0.3943	0.3357
17043.02	0.0058	0.0035	0.0759	2.4360	0.1475	0.8308	0.3886	0.3066
17046.44	0.0048	-0.0003	0.0821	2.5336	0.1520	0.7647	0.3989	0.3692
17049.86	0.0017	0.0052	0.0728	2.6166	0.1739	0.8533	0.3785	0.3643
17053.28	0.0052	0.0037	0.0844	2.5918	0.1545	0.8319	0.4325	0.3758
17056.70	0.0101	0.0022	0.0742	2.6012	0.1453	0.8289	0.4278	0.3314
17060.12	0.0056	0.0040	0.0776	2.6980	0.1556	0.8447	0.3979	0.4061
17063.54	0.0050	0.0031	0.0632	2.3996	0.1604	0.7519	0.3628	0.3529
17066.96	0.0031	0.0066	0.0686	2.6052	0.1655	0.8198	0.4016	0.3409
17070.38	0.0022	0.0025	0.0790	2.3687	0.1424	0.8140	0.4142	0.3328
17073.80	0.0047	0.0042	0.0815	2.4750	0.1401	0.7582	0.4173	0.3365
17077.22	0.0110	0.0051	0.0773	2.5931	0.1578	0.8323	0.4704	0.3317
17080.64	0.0030	0.0057	0.0748	2.5949	0.1531	0.8011	0.3857	0.3381
17084.06	0.0038	0.0012	0.0681	2.5833	0.1665	0.8198	0.4052	0.3263
17087.48	0.0039	0.0045	0.0703	2.4184	0.1561	0.8414	0.3744	0.3310
17090.90	0.0056	0.0041	0.0723	2.4434	0.1671	0.7713	0.4185	0.3113
17094.32	0.0039	0.0018	0.0653	2.4421	0.1571	0.8054	0.3819	0.3513
17097.74	0.0042	0.0022	0.0737	2.5639	0.1613	0.8247	0.4278	0.3692
17101.16	0.0046	0.0038	0.0661	2.4773	0.1496	0.7867	0.4290	0.3630
17104.58	0.0072	0.0004	0.0886	2.4555	0.1784	0.7804	0.4091	0.3300
17108.00	0.0056	0.0033	0.0727	2.6027	0.1582	0.8597	0.4067	0.3507
17111.42	0.0083	0.0061	0.0762	2.4582	0.1539	0.7594	0.4058	0.3330
17114.84	0.0045	-0.0003	0.0679	2.3854	0.1553	0.7629	0.3513	0.3523
17118.26	0.0059	0.0022	0.0742	2.6014	0.1655	0.7848	0.4276	0.3666
17121.68	0.0054	0.0046	0.0765	2.5957	0.1351	0.8484	0.3982	0.3624

17125.10	0.0055	0.0033	0.0605	2.4843	0.1348	0.7853	0.3999	0.3257
17128.52	0.0033	0.0063	0.0858	2.5253	0.1550	0.8103	0.4006	0.3207
17131.94	0.0094	0.0018	0.0891	2.6182	0.1831	0.8183	0.4067	0.3766
17135.36	0.0066	0.0011	0.0806	2.5574	0.1774	0.7876	0.3930	0.3476
17138.78	0.0028	0.0080	0.0619	2.4667	0.1488	0.7737	0.3973	0.3328
17142.20	0.0021	0.0068	0.0784	2.4251	0.1497	0.8091	0.3634	0.3209
17145.62	0.0056	0.0012	0.0849	2.7383	0.1632	0.8376	0.4664	0.3491
17149.04	0.0051	0.0030	0.0726	2.4988	0.1517	0.7612	0.3785	0.3484
17152.46	0.0035	0.0022	0.0827	2.7357	0.1801	0.8591	0.4425	0.3902
17155.88	0.0037	0.0042	0.0730	2.3341	0.1322	0.7809	0.3798	0.3547
17159.30	0.0059	0.0011	0.0788	2.4330	0.1621	0.7768	0.3282	0.3648
17162.72	0.0025	-0.0003	0.0723	2.5005	0.1737	0.7895	0.3843	0.3556
17166.14	0.0079	0.0051	0.0598	2.5114	0.1553	0.8345	0.4069	0.3267
17169.56	0.0041	0.0056	0.0649	2.4684	0.1599	0.7863	0.3905	0.3449
17172.98	0.0043	0.0025	0.0669	2.6167	0.1686	0.8421	0.4013	0.3432
17176.40	0.0054	0.0039	0.0740	2.6024	0.1664	0.8553	0.4436	0.3544
17179.82	0.0025	0.0021	0.0753	2.5932	0.1623	0.8221	0.4033	0.3286
17183.24	0.0032	0.0004	0.0834	2.5422	0.1485	0.8394	0.3991	0.3681
17186.66	0.0044	0.0046	0.0819	2.6725	0.1765	0.8428	0.4061	0.3282
17190.08	0.0060	0.0059	0.0797	2.6956	0.1697	0.8765	0.4233	0.3718
17193.50	0.0044	0.0022	0.0824	2.6853	0.1644	0.8269	0.4104	0.3661
17196.92	0.0028	0.0030	0.0694	2.4938	0.1259	0.7456	0.3705	0.3376
17200.34	0.0062	0.0037	0.0716	2.4878	0.1748	0.7982	0.4251	0.3499
17203.76	0.0059	-0.0002	0.0725	2.4207	0.1466	0.8047	0.3891	0.3541
17207.18	0.0071	0.0037	0.0795	2.5038	0.1706	0.8206	0.3952	0.3293
17210.60	0.0058	0.0017	0.0823	2.5232	0.1603	0.7855	0.3595	0.3193
17214.02	0.0056	0.0042	0.0638	2.4775	0.1445	0.7874	0.3989	0.3084
17217.44	0.0028	0.0073	0.0816	2.5418	0.1646	0.8020	0.4054	0.3611
17220.86	0.0059	0.0035	0.0670	2.3569	0.1528	0.8072	0.3832	0.3262
17224.28	0.0034	0.0046	0.0688	2.4595	0.1595	0.8601	0.3823	0.3280
17227.70	0.0032	0.0044	0.0846	2.5336	0.1582	0.8476	0.4115	0.3556
17231.12	0.0052	0.0020	0.0842	2.4555	0.1552	0.7968	0.3869	0.3421
17234.54	0.0027	0.0026	0.0755	2.4227	0.1653	0.8108	0.3804	0.3497
17237.96	0.0105	0.0049	0.0919	2.6298	0.1638	0.8179	0.3866	0.3728
17241.38	0.0050	0.0033	0.0693	2.4952	0.1657	0.8253	0.3518	0.3546
17244.80	0.0027	0.0086	0.0827	2.5769	0.1630	0.7904	0.3970	0.3458
17248.22	0.0046	0.0023	0.0733	2.4667	0.1621	0.8054	0.4047	0.3299
17251.64	0.0042	0.0047	0.0792	2.7060	0.1688	0.8172	0.4137	0.3522
17255.06	0.0049	0.0067	0.0781	2.5192	0.1724	0.8402	0.4203	0.3511
17258.48	0.0039	0.0031	0.0657	2.4591	0.1543	0.7750	0.3608	0.3480
17261.90	0.0026	0.0047	0.0732	2.3529	0.1475	0.7283	0.3714	0.3508
17265.32	0.0082	0.0061	0.0749	2.5051	0.1554	0.8055	0.3898	0.3257
17268.74	0.0063	0.0017	0.0668	2.5647	0.1490	0.8023	0.4087	0.3565
17272.16	0.0039	0.0066	0.0766	2.5073	0.1694	0.7898	0.3862	0.3239
17275.58	0.0038	0.0066	0.0634	2.5872	0.1491	0.8341	0.3862	0.3672

Experiment 25253 Xenon Isotopic Ratio Data

Time	$^{124}Xe/^{132}Xe$	$^{126}Xe/^{132}Xe$	$^{128}Xe/^{132}Xe$	$^{129}Xe/^{132}Xe$	$^{130}Xe/^{132}Xe$	$^{131}Xe/^{132}Xe$	$^{134}Xe/^{132}Xe$	$^{136}Xe/^{132}Xe$
14803.42	0.0061	-0.0002	0.1100	2.4491	0.1669	0.7960	0.3720	0.3641
14808.3	0.0009	0.0057	0.0565	2.5699	0.1596	0.7936	0.3718	0.3246
14813.18	0.0037	0.0038	0.0766	2.5643	0.1402	0.8408	0.4341	0.3232
14818.06	0.0070	0.0059	0.0628	2.4474	0.1555	0.7141	0.3852	0.3365
14822.94	0.0057	0.0004	0.0729	2.6685	0.1677	0.8729	0.4593	0.4178
14827.82	0.0020	0.0039	0.0684	2.5624	0.1717	0.8171	0.4058	0.3443
14832.7	0.0025	-0.0030	0.0677	2.6697	0.1607	0.8533	0.3791	0.3382
14837.58	0.0063	0.0051	0.0888	2.7488	0.1529	0.8679	0.4304	0.4083
14842.46	0.0069	0.0025	0.0718	2.4486	0.1681	0.7848	0.4247	0.3439
14847.34	0.0069	0.0053	0.0798	2.4787	0.1548	0.8489	0.3830	0.3464
14852.22	0.0049	0.0129	0.0814	2.6781	0.1535	0.8750	0.4575	0.4045
14857.1	0.0056	-0.0002	0.0799	2.4761	0.1299	0.8019	0.3774	0.3779
14861.98	0.0012	0.0003	0.0838	2.4539	0.1697	0.7835	0.4038	0.3235
14866.86	0.0044	0.0075	0.0952	2.4699	0.1481	0.8522	0.3778	0.3396
14871.74	0.0045	0.0003	0.0678	2.6033	0.1638	0.8119	0.3799	0.3915
14876.62	0.0052	0.0052	0.0827	2.4428	0.1591	0.8014	0.3998	0.3221
14881.5	0.0013	0.0072	0.0672	2.5429	0.1868	0.8234	0.3864	0.3715
14886.38	0.0039	0.0023	0.0765	2.6384	0.1604	0.7735	0.4043	0.3523
14891.26	0.0043	0.0003	0.0683	2.4693	0.1680	0.8296	0.3663	0.3268
14896.14	0.0032	0.0115	0.0731	2.5201	0.1347	0.8099	0.3691	0.3220
14901.02	0.0021	0.0040	0.0706	2.5274	0.1676	0.8359	0.3637	0.3111
14905.9	0.0051	0.0022	0.0700	2.4834	0.1368	0.7853	0.4335	0.3499
14910.78	0.0071	0.0085	0.0814	2.5604	0.1506	0.8040	0.3861	0.3555
14915.66	0.0061	0.0003	0.0735	2.5235	0.1596	0.8536	0.4319	0.3315
14920.54	0.0044	0.0012	0.0781	2.4129	0.1542	0.8115	0.3815	0.3577
14925.42	0.0039	0.0052	0.0737	2.3039	0.1660	0.7979	0.3597	0.3096
14930.3	0.0066	0.0041	0.0874	2.5332	0.1807	0.8365	0.4289	0.3472
14935.18	0.0084	0.0040	0.0729	2.6360	0.1714	0.8423	0.3899	0.3612
14940.06	0.0068	0.0081	0.0628	2.5684	0.1259	0.8289	0.3757	0.3337
14944.94	0.0051	0.0036	0.0813	2.6690	0.1442	0.8806	0.4137	0.4425
14949.82	0.0045	0.0087	0.0838	2.4112	0.1325	0.7396	0.3926	0.3497
14954.7	0.0055	0.0020	0.0769	2.3616	0.1502	0.7332	0.3815	0.2982
14959.58	0.0091	0.0020	0.0719	2.4433	0.1410	0.8041	0.3910	0.3477
14964.46	0.0092	0.0012	0.0803	2.7555	0.1755	0.8088	0.4595	0.3949
14969.34	0.0038	0.0077	0.0847	2.4455	0.1452	0.8197	0.3847	0.3458
14974.22	0.0058	0.0088	0.0836	2.4029	0.1742	0.7942	0.3563	0.3478
14979.1	0.0055	0.0072	0.0728	2.5998	0.1571	0.7908	0.4094	0.3316
14983.98	0.0071	0.0019	0.0661	2.5399	0.1642	0.7433	0.4107	0.3374
14988.86	0.0035	0.0060	0.0630	2.4260	0.1497	0.7517	0.4065	0.3599
14993.74	0.0078	-0.0020	0.0701	2.6735	0.1698	0.8409	0.3966	0.3670
14998.62	0.0038	0.0011	0.0803	2.7990	0.1707	0.8474	0.4223	0.3409

15003.5	0.0027	0.0039	0.0644	2.4509	0.1682	0.7528	0.3679	0.3209
15008.38	0.0033	0.0041	0.0711	2.2735	0.1618	0.7582	0.3562	0.3232
15013.26	0.0056	0.0068	0.0633	2.5633	0.1655	0.7800	0.4287	0.3266
15018.14	-0.0007	0.0063	0.0770	2.5032	0.1589	0.8118	0.3752	0.3619
15023.02	0.0028	0.0032	0.0909	2.6873	0.1700	0.8168	0.3871	0.3511
15027.9	0.0027	0.0043	0.0727	2.5005	0.1460	0.8173	0.4039	0.3477
15032.78	0.0018	0.0002	0.0816	2.4501	0.1571	0.7525	0.4067	0.3577
15037.66	0.0110	0.0021	0.0764	2.4491	0.1580	0.8005	0.3836	0.3324
15042.54	0.0051	0.0050	0.0686	2.4522	0.1807	0.8363	0.3642	0.3537
15047.42	0.0034	0.0026	0.0630	2.5183	0.1804	0.7913	0.3809	0.3613
15052.3	0.0083	0.0018	0.0648	2.6655	0.1551	0.8035	0.4181	0.3587
15057.18	0.0051	0.0034	0.0917	2.6091	0.1808	0.8403	0.4168	0.3385
15062.06	0.0070	0.0025	0.0712	2.5289	0.1347	0.8492	0.4077	0.3418
15066.94	0.0072	0.0025	0.0715	2.4857	0.1443	0.7753	0.3873	0.3261
15071.82	0.0001	0.0041	0.0767	2.5676	0.1728	0.8033	0.4062	0.3421
15076.7	0.0032	0.0009	0.0639	2.4989	0.1486	0.7668	0.4130	0.3178
15081.58	0.0032	0.0024	0.0674	2.4612	0.1600	0.8446	0.4005	0.3410
15086.46	0.0048	0.0025	0.0652	2.5875	0.1477	0.8507	0.4002	0.3639
15091.34	0.0032	0.0009	0.0835	2.4599	0.1407	0.8034	0.4214	0.3613
15096.22	0.0081	0.0033	0.0775	2.5965	0.1727	0.8460	0.4271	0.3603
15101.1	0.0036	0.0043	0.0710	2.5407	0.1450	0.8618	0.4084	0.3682
15105.98	0.0097	0.0056	0.0811	2.7163	0.1753	0.8213	0.4493	0.3752
15110.86	0.0038	0.0038	0.0710	2.5108	0.1596	0.7442	0.4061	0.3059
15115.74	0.0030	0.0005	0.0843	2.3894	0.1763	0.7935	0.3393	0.3169
15120.62	0.0026	0.0022	0.0781	2.4569	0.1541	0.7696	0.3877	0.3340
15125.5	0.0048	0.0008	0.0716	2.4621	0.1577	0.7928	0.3909	0.3615
15130.38	0.0064	0.0030	0.0805	2.6013	0.1905	0.8569	0.3964	0.3676
15135.26	0.0043	0.0018	0.0761	2.3799	0.1589	0.7612	0.3974	0.3286
15140.14	0.0066	0.0012	0.0897	2.4838	0.1723	0.8021	0.3864	0.3872
15145.02	0.0098	0.0054	0.0841	2.4733	0.1368	0.8370	0.4067	0.3227
15149.9	0.0031	0.0037	0.0807	2.5622	0.1393	0.8649	0.4393	0.3520
15154.78	0.0005	0.0036	0.0671	2.4628	0.1586	0.8134	0.3944	0.3336
15159.66	0.0034	0.0109	0.0876	2.6596	0.1523	0.8547	0.3680	0.3509

Experiment ID#25111 Krypton Isotopic Ratio Data

Time	^{80}Kr/^{84}/Kr	^{82}Kr/^{84}/Kr	^{83}Kr/^{84}/Kr	^{86}Kr/^{84}/Kr
16917.08	0.0624	0.2868	0.0805	0.2135
17394.48	0.0716	0.1497	0.1132	0.3029
17400.60	0.0587	0.2265	0.1278	0.2236
17406.72	0.0142	0.2213	0.1378	0.1975
17412.84	0.0452	0.1959	0.1929	0.2721
17418.96	0.0522	0.2188	0.2040	0.2702
17425.08	0.0693	0.1871	0.1947	0.2342
17431.20	0.0079	0.2946	0.2511	0.4051
17437.32	0.1263	0.1640	0.1751	0.2649
17443.44	0.1041	0.3425	0.1630	0.2124
17449.56	0.0642	0.2687	0.2640	0.4023
17455.68	0.1149	0.2655	0.2476	0.2809
17461.80	0.0649	0.2578	0.2683	0.2205
17467.92	0.0634	0.3680	0.2269	0.4234
17474.04	0.0768	0.2940	0.2770	0.3690
17480.16	0.1357	0.1452	0.2563	0.3757
17486.28	0.0486	0.2026	0.2339	0.3474
17492.40	0.0210	0.2401	0.2745	0.2023
17498.52	0.0608	0.2165	0.1319	0.2892
17504.64	0.0957	0.2060	0.1998	0.2733
17510.76	0.0870	0.2346	0.1897	0.3631
17516.88	0.0716	0.0882	0.1485	0.2055
17523.00	0.0215	0.1027	0.1320	0.2724
17529.12	0.0687	0.2755	0.2136	0.1832
17535.24	0.0032	0.1575	0.1970	0.3694
17541.36	0.0603	0.2261	0.1763	0.3472
17547.48	0.0605	0.1716	0.1616	0.2093
17553.60	0.1076	0.2365	0.2310	0.3409
17559.72	0.0290	0.4459	0.2790	0.3402
17565.84	0.0833	0.2651	0.2412	0.3487
17571.96	-0.0113	0.1603	0.2846	0.3567
17578.08	0.0660	0.2018	0.1315	0.2186
17584.20	0.0909	0.1335	0.2524	0.2588
17590.32	0.0398	0.1955	0.1763	0.2982
17596.44	0.1001	0.1793	0.2779	0.2837
17602.56	0.0294	0.1480	0.2027	0.3325
17608.68	0.0936	0.3463	0.1746	0.3834
17614.80	0.0217	0.2767	0.2119	0.3624
17620.92	0.0588	0.1773	0.1514	0.3636
17627.04	0.0335	0.1955	0.1949	0.2835
17633.16	0.1096	0.1720	0.2027	0.4036
17639.28	0.0509	0.2340	0.1369	0.2611
17676.48	0.0451	0.2413	0.2048	0.2973
17682.60	0.0548	0.2426	0.1951	0.2106
17688.72	0.1087	0.2193	0.1977	0.3193
17694.84	0.0596	0.1968	0.2047	0.2379
17700.96	0.0706	0.1181	0.2247	0.3988
17707.08	0.0352	0.1498	0.1399	0.3347
17713.20	0.0444	0.1648	0.1631	0.3418
17719.32	0.0510	0.1955	0.1502	0.2786

17725.44	0.0355	0.1982	0.1567	0.2470
17731.56	0.0920	0.2037	0.3273	0.3613
17737.68	0.0993	0.1921	0.2133	0.3060
17743.80	0.1336	0.1776	0.2509	0.4175
17749.92	0.1357	0.2750	0.2100	0.4365
17756.04	0.0291	0.1113	0.1909	0.1755
17762.16	0.0946	0.1353	0.1967	0.4022
17768.28	0.0309	0.2683	0.2537	0.3093
17774.40	0.0787	0.2145	0.2139	0.3156
17780.52	0.0603	0.2201	0.1567	0.2751
17786.64	0.0337	0.1840	0.2129	0.2470
17792.76	0.0351	0.2566	0.2089	0.2754
17798.88	0.1320	0.2097	0.2540	0.3370
17805.00	0.0710	0.1667	0.1641	0.2400
17811.12	0.1002	0.2426	0.2149	0.2389
17817.24	0.0729	0.1572	0.2563	0.3478
17823.36	0.0533	0.2996	0.2209	0.3211
17829.48	0.0414	0.2120	0.0934	0.2677
17835.60	0.0407	0.2117	0.2437	0.3597
17841.72	0.0556	0.2788	0.2124	0.2469
17847.84	0.0759	0.2293	0.2214	0.3266
17853.96	0.0409	0.3258	0.2218	0.4480
17860.08	0.1159	0.3476	0.2030	0.3941
17866.20	0.0579	0.2074	0.2562	0.2420
17872.32	0.0835	0.2066	0.3037	0.3365
17878.44	0.0725	0.2795	0.2038	0.2657
17884.56	0.0445	0.1256	0.2170	0.3177
17890.68	0.1800	0.1927	0.3101	0.3330
17896.80	0.1238	0.3722	0.2655	0.2440
17902.92	0.0201	0.2742	0.2478	0.2849
17909.04	0.1047	0.1860	0.1885	0.3109
17915.16	0.0993	0.2583	0.2083	0.3506
17921.28	0.0826	0.2230	0.2437	0.3197
18400.68	0.0585	0.2788	0.1786	0.2709
18406.80	0.0745	0.1802	0.2413	0.1976
18412.92	0.0658	0.1650	0.1922	0.2625
18419.04	0.0995	0.2490	0.2811	0.3919
18425.16	0.0509	0.1710	0.1903	0.3002
18431.28	0.0471	0.1715	0.1207	0.2800
18437.40	0.0878	0.2722	0.1991	0.3119
18443.52	0.0228	0.3157	0.1312	0.2476
18449.64	0.0626	0.1891	0.3014	0.2020
18455.76	0.0332	0.1891	0.2108	0.3989
18461.88	0.0722	0.2429	0.1541	0.3876
18468.00	0.0174	0.1833	0.2046	0.2679
18474.12	0.0790	0.3781	0.1493	0.2656
18480.24	0.0408	0.1763	0.1591	0.2302
18486.36	0.1004	0.2123	0.2317	0.2876
18492.48	0.1194	0.1613	0.1151	0.2569
18498.60	0.0423	0.1667	0.1814	0.2814
18504.72	0.0224	0.1069	0.2497	0.2097
18510.84	0.0126	0.2052	0.2216	0.4059
18516.96	0.0671	0.2656	0.0887	0.3113
18523.08	0.0898	0.1379	0.1248	0.2193

18529.20	0.0440	0.2021	0.1420	0.4120
18535.32	0.0569	0.2869	0.2076	0.3771
18541.44	0.0033	0.2543	0.1983	0.3425
18547.56	0.0664	0.2032	0.1557	0.2570
18553.68	-0.0054	0.2755	0.2159	0.3115
18559.80	0.1005	0.2606	0.2128	0.3055
18565.92	0.0612	0.3128	0.1546	0.3665
18572.04	0.0405	0.1488	0.1269	0.2570
18578.16	0.0715	0.2662	0.2973	0.3795
18584.28	0.0600	0.1808	0.2027	0.2642
18590.40	0.1455	0.1803	0.2641	0.3134
18596.52	0.1513	0.3578	0.3388	0.3365
18602.64	0.0040	0.1991	0.2371	0.3930
18608.76	0.0550	0.2574	0.1801	0.3079
18614.88	0.1759	0.2308	0.2914	0.3439
18621.00	0.0598	0.2406	0.2115	0.2942
18627.12	0.0495	0.3142	0.1504	0.3340
18633.24	0.0812	0.1884	0.1221	0.2590
18639.36	0.1025	0.2237	0.1880	0.3269
18645.48	0.0509	0.1925	0.1771	0.2486
18681.68	0.0613	0.1961	0.2706	0.2906
18687.80	0.0970	0.1331	0.2175	0.2967
18693.92	0.0468	0.2150	0.1912	0.2591
18700.04	0.0867	0.2269	0.2048	0.3439
18706.16	0.0452	0.2102	0.1843	0.3106
18712.28	0.0593	0.1264	0.1077	0.2651
18718.40	0.1006	0.3196	0.3248	0.4176
18724.52	0.0611	0.2239	0.1268	0.1462
18730.64	0.0510	0.2624	0.2667	0.3131
18736.76	0.0703	0.3441	0.1069	0.4385
18742.88	0.0642	0.1460	0.2359	0.3110
18749.00	0.0412	0.3045	0.0903	0.3013
18755.12	0.0715	0.3044	0.2229	0.1572
18761.24	0.0420	0.1620	0.2517	0.2792
18767.36	0.1005	0.1631	0.2599	0.3119
18773.48	0.1321	0.2275	0.3108	0.3539
18779.60	0.0703	0.3677	0.3071	0.2734
18785.72	0.1045	0.1641	0.1596	0.3603
18791.84	0.0933	0.1015	0.1887	0.3998
18797.96	0.0608	0.3441	0.2924	0.3973
18804.08	0.0763	0.2163	0.1958	0.4098
18810.20	0.0560	0.1473	0.1705	0.4518
18816.32	0.1280	0.1755	0.2065	0.2448
18822.44	0.0679	0.2959	0.2825	0.3290
18828.56	0.0412	0.2301	0.2327	0.3668
18834.68	0.0619	0.2601	0.2907	0.3648
18840.80	0.0706	0.1708	0.1421	0.3014
18846.92	0.0509	0.2831	0.2982	0.3495
18853.04	0.0336	0.2207	0.2589	0.3117
18859.16	0.0695	0.2093	0.2301	0.2675
18865.28	0.0748	0.2628	0.2545	0.3881
18871.40	0.0671	0.2091	0.2236	0.1823
18877.52	0.1131	0.2975	0.1558	0.3853
18883.64	0.0599	0.1978	0.1824	0.4053

18889.76	0.0563	0.1939	0.1516	0.3681
18895.88	0.0676	0.1836	0.1775	0.3498
18902.00	0.0350	0.1593	0.1502	0.2483
18908.12	0.0870	0.1854	0.1918	0.2528
18914.24	0.1131	0.2315	0.1809	0.3439
18920.36	0.1381	0.2666	0.1948	0.3372
18926.48	0.0633	0.3535	0.1978	0.3493
19402.88	0.0469	0.1758	0.2232	0.3155
19409.00	0.0482	0.2277	0.1906	0.2931
19415.12	0.0825	0.1849	0.1638	0.2410
19421.24	0.0689	0.2321	0.1534	0.3205
19427.36	0.0366	0.1274	0.1798	0.2317
19433.48	0.0453	0.1963	0.1931	0.3281
19439.60	0.0458	0.1182	0.1606	0.3492
19445.72	0.0346	0.1802	0.2142	0.3204
19451.84	0.0693	0.2495	0.1498	0.2326
19457.96	0.0738	0.2264	0.1847	0.3474
19464.08	0.1263	0.2055	0.1475	0.3715
19470.20	0.1268	0.2817	0.1806	0.3266
19476.32	0.0654	0.2475	0.2701	0.3567
19482.44	0.0980	0.2313	0.1460	0.3194
19488.56	0.0260	0.1704	0.1612	0.2649
19494.68	0.0406	0.2387	0.2391	0.3947
19500.80	0.0641	0.2321	0.1671	0.4513
19506.92	0.0466	0.1287	0.2353	0.3073
19513.04	0.0342	0.2523	0.2574	0.4675
19519.16	0.0965	0.2260	0.2536	0.3795
19525.28	0.0876	0.1844	0.2480	0.3438
19531.40	0.0566	0.2234	0.1886	0.3865
19537.52	0.0421	0.1879	0.1652	0.3601
19543.64	0.0670	0.2174	0.2566	0.2756
19549.76	0.0608	0.2203	0.0966	0.2827
19555.88	0.0529	0.2003	0.1637	0.2683
19562.00	0.0775	0.1759	0.1541	0.3267
19568.12	0.0487	0.3129	0.2443	0.3993
19574.24	0.0494	0.1756	0.1606	0.2383
19580.36	0.1145	0.2053	0.2303	0.3402
19586.48	0.0384	0.3163	0.3401	0.3652
19592.60	0.0526	0.2383	0.1852	0.3176
19598.72	0.0325	0.1891	0.1381	0.3307
19604.84	0.0310	0.2920	0.2415	0.3231
19610.96	0.0730	0.2146	0.2677	0.3063
19617.08	0.0728	0.1176	0.1651	0.2830
19623.20	0.0214	0.1254	0.1533	0.2914
19629.32	0.0651	0.3398	0.1492	0.3029
19635.44	0.0994	0.1679	0.2027	0.2095
19641.56	0.0472	0.2090	0.2522	0.3213
19647.68	0.0603	0.2032	0.2228	0.3630
19684.88	0.0610	0.2112	0.2513	0.3172
19691.00	0.0760	0.2465	0.1696	0.5140
19697.12	0.0705	0.1811	0.1596	0.2533
19703.24	0.0689	0.2380	0.1564	0.2680
19709.36	0.0484	0.2366	0.1579	0.3629
19715.48	0.0884	0.1904	0.1741	0.3475

19721.60	0.0759	0.2337	0.2028	0.3017
19727.72	0.0737	0.2822	0.2627	0.2949
19733.84	0.0372	0.2390	0.2173	0.2926
19739.96	0.0795	0.1947	0.2146	0.3142
19746.08	0.1349	0.2051	0.2607	0.3339
19752.20	0.0403	0.1569	0.1864	0.2002
19758.32	0.0610	0.1772	0.1817	0.3061
19764.44	0.0555	0.2645	0.1725	0.2930
19770.56	0.0654	0.2631	0.1218	0.3337
19776.68	0.1052	0.2265	0.1806	0.4196
19782.80	0.1098	0.3157	0.2816	0.4668
19788.92	0.0425	0.1845	0.1511	0.3023
19795.04	0.0879	0.1990	0.1423	0.4335
19801.16	0.0768	0.2399	0.2097	0.3801
19807.28	0.0469	0.2112	0.1801	0.3744
19813.40	0.0546	0.1845	0.0960	0.1826
19819.52	0.0711	0.2304	0.1795	0.3213
19825.64	0.0549	0.2573	0.1426	0.2767
19831.76	0.0454	0.2835	0.2674	0.4374
19837.88	0.0620	0.2208	0.1618	0.2502
19844.00	0.0683	0.1706	0.1709	0.3714
19850.12	0.0490	0.1676	0.2581	0.3255
19856.24	0.0569	0.3273	0.2659	0.3416
19862.36	0.0663	0.2401	0.1729	0.2537
19868.48	0.0919	0.1574	0.2164	0.3342
19874.6	0.0376	0.1766	0.2007	0.1900
19880.72	0.0802	0.2501	0.2023	0.3725
19886.84	0.1071	0.2027	0.2189	0.3334
19892.96	0.0497	0.2361	0.2115	0.2272
19899.08	0.0432	0.3117	0.2094	0.2708
19905.2	0.0331	0.1842	0.1564	0.3793
19911.32	0.0319	0.1438	0.2272	0.2205
19917.44	0.0292	0.1518	0.1025	0.3305
19923.56	0.0905	0.1756	0.2690	0.2888
19929.68	0.0372	0.3108	0.1668	0.2711

Experiment 25269 Krypton Isotopic Ratio Data

Time	^{80}Kr/^{84}Kr	^{82}Kr/^{84}Kr	^{83}Kr/^{84}Kr	^{86}Kr/^{84}Kr
18357.16	-0.0021	0.1086	0.2016	0.1668
18359.76	0.0749	0.2390	0.1871	0.0865
18362.36	0.0710	0.1571	0.2678	0.2813
18364.96	0.0718	0.1306	0.1035	0.1257
18367.56	0.0135	0.2354	0.3125	0.3489
18370.16	0.1485	0.2151	0.3388	0.2183
18372.76	0.1921	0.2801	0.1269	0.3885
18375.36	0.0539	0.3129	0.1811	0.2568
18377.96	0.0419	0.3171	0.0766	0.2161
18380.56	0.0497	0.2512	0.2920	0.4921
18383.16	0.0372	0.2406	0.1810	0.3123
18385.76	0.0137	0.1892	0.0764	0.2135
18388.36	0.0758	0.2210	0.1166	0.5461
18390.96	0.1403	0.0775	0.2140	0.4093
18393.56	-0.0517	0.3175	0.3392	0.3928
18396.16	-0.0529	0.1855	0.1858	0.2737
18398.76	0.0755	0.0957	0.1594	0.2043
18401.36	-0.0066	0.2689	0.3991	0.1369
18403.96	0.1175	0.2722	0.3926	0.2123
18406.56	0.1971	0.4892	0.2743	0.4552
18409.16	0.0795	0.2925	0.1523	0.2437
18411.76	0.1372	0.2629	0.4691	0.4603
18414.36	0.1491	0.1837	0.1380	0.1367
18416.96	0.0536	0.3630	0.2155	0.3493
18419.56	0.1775	0.4077	0.2019	0.4703
18422.16	0.0490	0.2751	0.0451	0.1993
18424.76	0.0836	0.0847	0.2714	0.2395
18427.36	0.0533	0.2269	0.1776	0.0818
18429.96	0.1801	0.3915	0.3728	0.4653
18432.56	0.0907	0.2237	0.0672	0.3945
18435.16	0.0267	0.1593	0.2072	0.3551
18437.76	0.1005	0.2867	0.3010	0.4104
18440.36	0.1472	0.2714	0.2029	0.4093
18442.96	0.0882	0.1768	0.3546	0.3245
18445.56	0.0882	0.2535	0.1479	0.5095
18448.16	0.0915	0.2401	0.2014	0.3705
18450.76	0.1125	0.0925	0.2209	0.2041
18453.36	0.0531	0.1993	0.1922	0.4489
18455.96	-0.0102	0.2645	0.2214	0.3073
18458.56	0.0205	0.3542	0.3794	0.4457
18461.16	0.1054	0.3571	0.1347	0.3112

18463.76	0.0745	0.3094	0.2884	0.2974
18466.36	0.0987	0.3187	0.1682	0.2287
18468.96	0.0964	0.3893	0.3304	0.3487
18471.56	0.0547	0.2153	0.2104	0.1438
18474.16	0.0910	0.2677	0.1127	0.1661
18476.76	0.0254	0.1851	0.2100	0.2112
18479.36	0.0892	0.2530	0.1748	0.2877
18481.96	0.0461	0.1348	0.2922	0.1901
18484.56	0.0949	0.1608	0.1521	0.2456
18487.16	0.1887	0.2003	0.1164	0.3837
18489.76	-0.0113	0.2451	0.3219	0.2734
18492.36	0.1140	0.1165	0.0817	0.3768
18494.96	0.0584	0.1112	0.2271	0.2544
18497.56	0.1160	0.1992	0.2598	0.2082
18500.16	0.0084	0.1355	0.2067	0.1461
18502.76	0.0496	0.2216	0.0927	0.2384
18505.36	0.0220	0.1839	0.2069	0.2508
18507.96	0.0781	0.2393	0.1542	0.1394
18510.56	0.0568	0.1990	0.1748	0.3734
18513.16	0.0339	0.2589	0.1801	0.3161
18515.76	0.1311	0.2439	0.2011	0.3110
18518.36	0.0958	0.1427	0.1354	0.1411
18520.96	0.1032	0.1479	0.3266	0.3974
18523.56	0.1108	0.2677	0.2959	0.4218
18526.16	0.0065	0.2243	0.1277	0.3427
18528.76	0.1090	0.1507	0.0787	0.2632
18531.36	0.0650	0.2437	0.2342	0.4445
18533.96	0.0847	0.1282	0.2741	0.3619
18536.56	0.0403	0.1148	0.2112	0.2967
18539.16	0.0626	0.1747	0.1546	0.1278
18541.76	0.0689	0.1686	0.2078	0.2318
18544.36	0.1445	0.2660	0.1964	0.3741
18546.96	0.0869	0.1940	0.1769	0.2074
18549.56	0.0002	0.1505	0.2291	0.2557
18552.16	0.0288	0.2052	0.1752	0.2602
18554.76	0.0402	0.2789	0.1689	0.2975
18557.36	0.0461	0.3365	0.2197	0.2362
18559.96	0.0334	0.3819	0.1658	0.2692
18562.56	0.1819	0.2496	0.1780	0.2801
18565.16	0.1320	0.1657	0.1508	0.2527
18567.76	0.0867	0.3187	0.2892	0.3933
18570.36	0.0463	0.1555	0.1722	0.2911
18572.96	0.2002	0.3393	0.2637	0.2936
18575.56	0.0729	0.1989	0.2388	0.1375

18578.16	0.0432	0.1507	0.1856	0.3228
18580.76	0.0623	0.1136	0.0982	0.3566
18583.36	0.0713	0.1275	0.2478	0.3316
18585.96	0.0268	0.0892	0.1323	0.2667
18588.56	0.0364	0.3402	0.1723	0.3885
18591.16	0.2155	0.2243	0.3530	0.5634
18593.76	0.1092	0.1169	0.1605	0.3709
18596.36	0.0927	0.2167	0.1605	0.2547
18598.96	-0.0235	0.2486	0.1041	0.3849
18601.56	0.0440	0.1941	0.3018	0.3103
18604.16	0.0343	0.1986	0.0933	0.1929
18606.76	0.0134	0.1958	0.1411	0.2546
18609.36	0.1634	0.2766	0.2431	0.3531
18611.96	0.0094	0.0664	0.0905	0.4236
18614.56	0.1234	0.1202	0.3647	0.3340
18617.16	0.1007	0.1887	0.0955	0.2961
18619.76	0.0505	0.2099	0.2009	0.3261
18622.36	0.0558	0.1375	0.1551	0.2128
18624.96	0.0713	0.0823	0.1898	0.2329
18627.56	0.0144	0.1569	0.0796	0.2174
18630.16	0.0410	0.1205	0.2624	0.1904
18632.76	0.1228	0.2243	0.2176	0.3561
18635.36	0.0078	0.1874	0.2284	0.2769
18637.96	0.0971	0.2114	0.1997	0.2565
18640.56	0.0377	0.1943	0.0773	0.3853
18643.16	0.0606	0.1839	0.1206	0.2724
18645.76	0.0744	0.1408	0.2244	0.2867
18648.36	0.0458	0.1928	0.1953	0.3021
18650.96	0.1061	0.3767	0.2225	0.2851
18653.56	0.0633	0.1930	0.1831	0.2864
18656.16	0.0680	0.2717	0.1082	0.4006
18658.76	0.0851	0.2342	0.2616	0.2068
18661.36	0.1014	0.1764	0.1754	0.3262
18663.96	0.0795	0.1841	0.2338	0.4106
18666.56	0.0475	0.2807	0.1729	0.3660
18669.16	0.0798	0.2568	0.2674	0.2629
18671.76	0.0963	0.2269	0.3119	0.4843
18674.36	0.0356	0.2483	0.2406	0.1216
18676.96	0.0265	0.0937	0.2236	0.1270
18679.56	0.0477	0.2295	0.2666	0.2907
18682.16	0.0758	0.2289	0.2232	0.2848
18684.76	0.0481	0.1482	0.1382	0.1979
18687.36	0.0550	0.1441	0.2225	0.2626
18689.96	0.1183	0.2285	0.2384	0.3627

18692.56	0.0352	0.1867	0.1802	0.2727
18695.16	0.0716	0.1283	0.1774	0.2679
18697.76	0.0922	0.2788	0.2722	0.2817
18700.36	0.0952	0.1423	0.1749	0.2270
18702.96	0.0706	0.1381	0.3152	0.1891
18705.56	0.0855	0.1823	0.1022	0.2737
18708.16	0.0217	0.2096	0.1504	0.3456
18710.76	0.0679	0.2001	0.2095	0.3209
18713.36	0.1782	0.1546	0.3196	0.4871
18715.96	0.1512	0.1856	0.1514	0.3777
18718.56	0.0635	0.1891	0.1479	0.3016
18721.16	0.0398	0.1896	0.1626	0.2863
18723.76	0.0735	0.1271	0.1378	0.2829
18726.36	0.0963	0.2695	0.0210	0.3113
18728.96	0.1293	0.1792	0.1799	0.2570
18731.56	0.0775	0.2504	0.3085	0.3472
18734.16	0.0915	0.1375	0.1102	0.1922
18736.76	0.0145	0.1839	0.2217	0.3676
18739.36	0.0512	0.3666	0.1345	0.3902
18741.96	0.0702	0.1459	0.3120	0.3344
18744.56	0.0682	0.2471	0.0912	0.1929
18747.16	0.0751	0.1624	0.2471	0.2921
18749.76	0.0453	0.1998	0.1796	0.2462
18752.36	0.0794	0.2274	0.1700	0.3746
18754.96	0.1367	0.2435	0.1157	0.2539
18757.56	0.0865	0.2962	0.1979	0.2566
18760.16	0.0284	0.2016	0.2001	0.1621
18762.76	0.0480	0.2784	0.1303	0.2933
18765.36	0.0604	0.1962	0.1837	0.2173
18767.96	0.0631	0.0490	0.1912	0.2501
18770.56	0.0266	0.1809	0.1566	0.2549
18773.16	0.0722	0.2443	0.3068	0.4107
18775.76	0.1079	0.2472	0.3411	0.2242
18778.36	0.0449	0.1900	0.2368	0.2614
18780.96	0.0514	0.1006	0.3069	0.2948
18783.56	0.0508	0.1044	0.1188	0.2197
18786.16	0.0923	0.2708	0.2962	0.3672
18788.76	0.0360	0.2044	0.2498	0.2959
18791.36	0.1908	0.1506	0.1390	0.3678
18793.96	0.0971	0.2676	0.1726	0.4703
18796.56	0.1404	0.1204	0.2774	0.3789
18799.16	0.1353	0.1566	0.1877	0.5430
18801.76	0.0657	0.3116	0.2068	0.3553
18804.36	0.1284	0.2193	0.3447	0.4608

18806.96	0.0330	0.1643	0.2567	0.2664
18809.56	0.0750	0.0842	0.2502	0.2984
18812.16	0.0966	0.1425	0.1781	0.1463
18814.76	0.0401	0.2291	0.2656	0.3055
18817.36	0.2219	0.3338	0.2071	0.2788
18819.96	0.0725	0.1807	0.1435	0.2859
18822.56	0.0135	0.1512	0.2882	0.4215
18825.16	0.0428	0.2013	0.1663	0.3629
18827.76	0.0874	0.2728	0.2359	0.3678
18830.36	0.0744	0.1161	0.2775	0.2202
18832.96	0.0435	0.1148	0.1641	0.1828
18835.56	-0.0002	0.3139	0.1571	0.2769
18838.16	0.0690	0.1148	0.1998	0.2822
18840.76	0.1422	0.2536	0.1933	0.3025
18843.36	0.0417	0.1702	0.1182	0.2426
18845.96	0.0095	0.2188	0.2316	0.3139
18848.56	0.0372	0.2066	0.1931	0.1861
18851.16	0.0063	0.1806	0.1615	0.3837
18853.76	0.0844	0.1818	0.1736	0.4075
18856.36	0.0356	0.1838	0.1550	0.2116
18858.96	0.1215	0.1916	0.2141	0.2631
18861.56	0.0166	0.1757	0.1798	0.3699
18864.16	0.0802	0.2153	0.2396	0.2881
18866.76	0.0679	0.1487	0.0951	0.2501
18869.36	0.0658	0.1915	0.2551	0.3320
18871.96	0.0899	0.2772	0.1588	0.3749
18874.56	0.0398	0.2284	0.1032	0.2592
18877.16	0.0958	0.3007	0.2147	0.2009
18879.76	0.1280	0.1757	0.2278	0.3146
18882.36	0.0775	0.1114	0.1289	0.1344
18884.96	0.0949	0.2128	0.1645	0.2160
18887.56	0.0123	0.2691	0.2111	0.2841
18890.16	0.1291	0.2456	0.3379	0.3712
18892.76	0.1100	0.1911	0.2245	0.3227
18895.36	0.0466	0.2110	0.2205	0.3020
18897.96	0.0834	0.2115	0.2402	0.2207
18900.56	0.0045	0.1654	0.1663	0.3677
18903.16	0.1018	0.1969	0.1601	0.3198
18905.76	0.0470	0.2351	0.2672	0.2319
18908.36	0.1167	0.2706	0.2643	0.2627
18910.96	0.0327	0.0743	0.1393	0.1590
18913.56	0.0441	0.1739	0.1486	0.3622
18916.16	0.1146	0.0834	0.2131	0.2161
18918.76	0.0421	0.1960	0.1416	0.2520

18921.36	0.0198	0.1354	0.1638	0.2801
18923.96	0.0742	0.1626	0.1969	0.2772
18926.56	0.0741	0.1908	0.2372	0.3559
18929.16	0.0886	0.2156	0.2766	0.2916
18931.76	0.0936	0.2607	0.1554	0.3216
18934.36	0.1697	0.2254	0.1033	0.2790
18936.96	0.0765	0.1862	0.1755	0.1946
18939.56	0.0578	0.3034	0.2901	0.2679
18942.16	0.0781	0.1606	0.1790	0.3783
18944.76	0.0812	0.2182	0.2826	0.2754
18947.36	0.0373	0.2516	0.2438	0.3310
18949.96	0.0637	0.1669	0.2004	0.4393
18952.56	0.1247	0.2773	0.1661	0.1728
18955.16	0.1110	0.2620	0.1709	0.2196
18957.76	0.0873	0.2627	0.2390	0.2909
18960.36	0.1076	0.1998	0.2947	0.2463
18962.96	0.1257	0.2530	0.2172	0.3643
18965.56	0.1061	0.1697	0.1501	0.4462
18968.16	0.0878	0.1750	0.1593	0.2605
18970.76	0.0407	0.2721	0.2529	0.4659
18973.36	0.0969	0.2123	0.1099	0.2014
18975.96	0.0835	0.2224	0.2570	0.2641
18978.56	0.0630	0.2192	0.2273	0.2428
18981.16	0.1390	0.1928	0.1358	0.3413
18983.76	0.0691	0.1984	0.0967	0.2294
18986.36	0.0982	0.2091	0.1530	0.3081
18988.96	0.0853	0.2427	0.1745	0.2766
18991.56	0.1584	0.2239	0.2414	0.2335
18994.16	0.0439	0.1471	0.1642	0.2282
18996.76	0.0996	0.1906	0.1978	0.2744
18999.36	0.0358	0.2522	0.3195	0.4298
19001.96	0.1421	0.1732	0.1497	0.2569
19004.56	0.0695	0.2254	0.1565	0.2087
19007.16	0.0386	0.2010	0.1544	0.3067
19009.76	0.0349	0.0646	0.1478	0.2909
19012.36	0.1359	0.2234	0.2122	0.3288
19014.96	0.0945	0.1901	0.2089	0.3242
19017.56	0.0445	0.2479	0.1752	0.3433
19020.16	0.1099	0.2562	0.2096	0.1663
19022.76	0.0628	0.2606	0.2147	0.3056
19025.36	0.1203	0.2238	0.2426	0.2346
19027.96	0.0802	0.1881	0.2247	0.2825
19030.56	0.0448	0.2529	0.1743	0.3604
19033.16	0.0710	0.2324	0.2162	0.2817

19035.76	0.1281	0.2782	0.2247	0.2436
19038.36	0.0567	0.2449	0.1640	0.1404
19040.96	0.0619	0.0834	0.1678	0.3661
19043.56	0.1132	0.2222	0.2315	0.2270
19046.16	0.1607	0.1148	0.1661	0.2564
19048.76	0.1078	0.1178	0.1118	0.1491
19051.36	0.0137	0.1735	0.1632	0.2651
19053.96	0.0733	0.1803	0.2806	0.3898
19056.56	0.0771	0.1734	0.2113	0.3085
19059.16	0.1332	0.1733	0.2053	0.3577
19061.76	0.0813	0.1897	0.2015	0.2265
19064.36	0.1473	0.1848	0.2406	0.1743
19066.96	0.0489	0.2681	0.1091	0.2376
19069.56	0.0680	0.1408	0.1514	0.2368
19072.16	0.0697	0.2347	0.0851	0.2328
19074.76	0.1018	0.2713	0.2793	0.3949
19077.36	0.0986	0.1666	0.1974	0.2986
19079.96	0.0876	0.2339	0.1692	0.2988
19082.56	0.1252	0.1592	0.1941	0.2623
19085.16	0.0416	0.2305	0.1300	0.2832
19087.76	0.1064	0.1590	0.1871	0.2032
19090.36	0.1113	0.1453	0.2179	0.3332
19092.96	0.1328	0.2037	0.2642	0.2586
19095.56	0.0374	0.2914	0.1645	0.4701
19098.16	0.0937	0.2251	0.2042	0.3287
19100.76	0.0827	0.2281	0.1894	0.2347
19103.36	0.0761	0.1910	0.1885	0.1762
19105.96	0.1562	0.2316	0.1103	0.2702
19108.56	0.0348	0.1843	0.0931	0.2976
19111.16	0.0608	0.2355	0.1022	0.3085
19113.76	0.0843	0.2539	0.2617	0.3798
19116.36	0.0553	0.1106	0.1579	0.3596
19118.96	0.1573	0.1726	0.2122	0.4540
19121.56	0.0433	0.2475	0.1855	0.3121
19124.16	0.0464	0.1707	0.2392	0.3275
19126.76	0.0762	0.3177	0.3233	0.4175
19129.36	0.0129	0.1703	0.2151	0.2678
19131.96	0.0331	0.2281	0.2197	0.2717
19134.56	0.0694	0.3103	0.2683	0.2861
19137.16	0.0508	0.3669	0.2795	0.3725
19139.76	0.0793	0.2268	0.1694	0.2352
19142.36	0.1067	0.2187	0.2149	0.2948
19144.96	0.0665	0.3384	0.1824	0.3331
19147.56	0.0580	0.2363	0.2769	0.3168

19150.16	0.0858	0.2853	0.1832	0.4387
19152.76	0.1289	0.2469	0.3004	0.2600
19155.36	0.0785	0.1530	0.2426	0.2770
19157.96	0.0648	0.2192	0.3735	0.3825
19160.56	0.1071	0.1957	0.1670	0.2305
19163.16	0.0902	0.3662	0.2408	0.3112
19165.76	0.0241	0.3342	0.2156	0.4097
19168.36	0.0441	0.2338	0.2490	0.3711
19170.96	0.0543	0.2123	0.1347	0.3147
19173.56	0.1164	0.1831	0.2616	0.4149
19176.16	0.0612	0.2772	0.3079	0.3026
19178.76	0.0593	0.1424	0.0721	0.3247
19181.36	0.0932	0.1902	0.0919	0.2967
19183.96	0.0304	0.2886	0.1841	0.3403
19186.56	0.1151	0.1585	0.2049	0.2812
19189.16	0.0774	0.1796	0.1217	0.3101
19191.76	0.1088	0.1689	0.2230	0.3850
19194.36	0.0427	0.2211	0.2183	0.3017
19196.96	0.0199	0.2144	0.1728	0.3197
19199.56	0.0314	0.2413	0.1335	0.3035
19202.16	0.0786	0.1559	0.2922	0.2972
19204.76	0.1167	0.3561	0.1724	0.3760
19207.36	0.0658	0.2280	0.1299	0.2520
19209.96	0.0978	0.1514	0.2271	0.2314
19212.56	0.0918	0.2103	0.1000	0.2993
19215.16	0.1541	0.2436	0.2163	0.4201
19217.76	0.1346	0.2701	0.1972	0.2448
19220.36	0.0999	0.1805	0.1621	0.2230
19222.96	0.0967	0.1513	0.2784	0.3136
19225.56	0.0318	0.2240	0.2069	0.2377
19228.16	0.1052	0.1332	0.1352	0.3154
19230.76	0.0962	0.2083	0.1247	0.2490
19233.36	0.0026	0.2266	0.2143	0.3589
19235.96	0.1040	0.2724	0.1595	0.3561
19238.56	0.0587	0.1986	0.1608	0.2268
19241.16	0.0215	0.2122	0.2724	0.3465
19243.76	0.1031	0.1680	0.0921	0.3833
19246.36	0.0778	0.2842	0.2478	0.3702
19248.96	0.1121	0.2630	0.2093	0.3940
19251.56	0.0936	0.1872	0.1945	0.3589
19254.16	0.1044	0.1817	0.2934	0.3363
19256.76	0.0411	0.3128	0.2556	0.3262
19259.36	0.1425	0.1082	0.1791	0.2426
19261.96	0.0581	0.1391	0.1477	0.2485

19264.56	0.1069	0.2101	0.1905	0.2329
19267.16	0.0501	0.1403	0.0998	0.3146
19269.76	0.0974	0.2763	0.1423	0.2240
19272.36	0.0890	0.2644	0.2749	0.2405
19274.96	0.0506	0.2066	0.2843	0.3340
19277.56	0.0811	0.2857	0.1378	0.3674
19280.16	0.0328	0.2958	0.1846	0.1708
19282.76	0.0522	0.0926	0.2402	0.2311
19285.36	0.0692	0.2591	0.2224	0.2514
19287.96	0.0441	0.2247	0.2651	0.2561
19290.56	0.0914	0.2903	0.2239	0.3478
19293.16	0.0998	0.2635	0.2075	0.3323
19295.76	0.0897	0.2402	0.1866	0.2631
19298.36	0.1940	0.2321	0.2555	0.2688
19300.96	0.0634	0.2639	0.3428	0.3698
19303.56	0.0919	0.2072	0.1646	0.3560
19306.16	0.0818	0.1788	0.1535	0.2654
19308.76	0.1088	0.1719	0.2023	0.2927
19311.36	0.0769	0.1998	0.1951	0.2112
19313.96	0.0682	0.1549	0.1986	0.2773
19316.56	0.1347	0.1320	0.2309	0.3839
19319.16	0.0874	0.2782	0.1952	0.3248
19321.76	0.0996	0.2993	0.2254	0.3520
19324.36	0.0658	0.1812	0.2080	0.3697
19326.96	0.0677	0.1946	0.2032	0.4005
19329.56	0.1287	0.2458	0.2047	0.3127
19332.16	0.0784	0.2042	0.2130	0.2608
19334.76	0.0678	0.2534	0.2223	0.3568
19337.36	0.0833	0.3042	0.2532	0.3095
19339.96	0.0840	0.1952	0.2365	0.2171
19342.56	0.1627	0.1943	0.2073	0.3848
19345.16	0.0832	0.2957	0.2494	0.3796
19347.76	0.1248	0.3176	0.2666	0.2803
19350.36	0.1258	0.2340	0.2288	0.3318
19352.96	0.0702	0.1383	0.2183	0.2885
19355.56	0.1187	0.2875	0.2351	0.3740
19358.16	0.0663	0.1887	0.1767	0.3728
19360.76	0.0703	0.1919	0.2497	0.2234
19363.36	0.0527	0.2981	0.1893	0.4656
19365.96	0.0945	0.2354	0.1364	0.3000
19368.56	0.0984	0.2262	0.2798	0.2424
19371.16	0.1192	0.1786	0.1775	0.1688
19373.76	0.0551	0.2133	0.2070	0.2989
19376.36	0.0473	0.2450	0.2387	0.3654

19378.96	0.1182	0.2168	0.2557	0.4423
19381.56	0.0737	0.1321	0.2975	0.2711
19384.16	0.0424	0.1361	0.1165	0.2017
19386.76	0.1472	0.1784	0.1651	0.3602
19389.36	0.0731	0.3149	0.1607	0.2944
19391.96	0.0740	0.1864	0.1272	0.2310
19394.56	0.1103	0.1989	0.2286	0.3842
19397.16	0.0719	0.1627	0.1643	0.3207
19399.76	0.0446	0.2384	0.1939	0.2874
19402.36	0.0394	0.1143	0.2487	0.3264
19404.96	0.0344	0.1789	0.0934	0.3476
19407.56	0.0802	0.1954	0.1162	0.2348
19410.16	0.0486	0.3380	0.1909	0.1807
19412.76	0.0841	0.1472	0.2643	0.2959
19415.36	0.0353	0.1817	0.2213	0.2238
19417.96	0.1350	0.1707	0.2039	0.3806
19420.56	0.1133	0.2343	0.1968	0.3620
19423.16	0.1019	0.1113	0.2426	0.2618
19425.76	0.0468	0.1478	0.3034	0.1915
19428.36	0.0991	0.2268	0.2443	0.2816
19430.96	0.0444	0.1622	0.1872	0.2984
19433.56	0.0808	0.1215	0.1529	0.1657
19436.16	0.0600	0.2718	0.1693	0.4312
19438.76	0.0694	0.3262	0.1528	0.2737
19441.36	0.1020	0.2851	0.2736	0.2688
19443.96	0.0878	0.1270	0.1753	0.3382
19446.56	0.0579	0.2361	0.1599	0.2184
19449.16	0.0817	0.1167	0.1762	0.3972
19451.76	0.0405	0.3078	0.1844	0.2452
19454.36	0.0605	0.1039	0.1598	0.3029
19474.20	0.0735	0.2260	0.2889	0.4073
19503.94	0.1084	0.2693	0.2062	0.2275
19533.68	0.1027	0.3187	0.2008	0.3526
19563.42	0.1252	0.2558	0.1449	0.2620
19593.16	0.0897	0.2071	0.2120	0.3198
19622.90	0.0269	0.2135	0.1414	0.3378
19652.64	0.0810	0.1563	0.3399	0.3368
19682.38	0.1131	0.2155	0.2180	0.3252
19712.12	0.0491	0.1417	0.2929	0.4234